

A Modal One-Way Navier-Stokes Approach to Modelling Non-Modal Boundary Layer Instabilities

Elliot J. Badcock^{1*} and Shahid Mughal¹

¹Department of Mathematics, Imperial College London, South Kensington Campus, London, SW7 2AZ, United Kingdom.

*Corresponding author(s). E-mail(s): ejb321@ic.ac.uk;
Contributing authors: s.mughal@imperial.ac.uk;

Abstract

This paper presents a method to solve the *modal* form of the linearised one-way Navier-Stokes (OWNS) equations for investigating disturbance development in developing subsonic and supersonic boundary layers. The modal framework offers significant advantages in robustness and computational efficiency over the conventional non-modal OWNS framework. Notably, we demonstrate that modal OWNS (M-OWNS) retains the capability to capture non-modal disturbance development. Our technique leverages the modal ansatz of parabolised stability equations (PSE) whilst employing the recursion-parameter parabolisation strategy of non-modal OWNS to stabilise the streamwise-marching modal algorithm. A key contribution is that we overcome the minimum streamwise step-size requirement that constrains conventional PSE in capturing short-scale disturbance evolution. We demonstrate through canonical test cases that fine-scale variations in the baseflow can be captured effectively. The M-OWNS procedure permits arbitrarily small streamwise-marching step-sizes whilst maintaining stability. Crucially, we find the algorithm to be more robust than conventional non-modal OWNS, whilst recovering identical modal and non-modal phenomena.

Keywords: Boundary layer instability, Parabolised Stability Equations (PSE), One-Way Navier-Stokes

1 Introduction

Modelling hydrodynamic instabilities and disturbance evolution in laminar boundary layers has advanced considerably over the past few decades, from both computational and physical-fidelity perspectives. Computational methods have progressed from local eigenvalue analyses

to comprehensive global approaches, encompassing both eigenvalue decomposition and forced harmonic response within non-modal Navier-Stokes frameworks. At the highest fidelity, global (TriGlobal) stability analysis solves the fully elliptic linear harmonic Navier-Stokes equations (LHNS) in every spatial direction, capturing both upstream and downstream disturbance dynamics [1, 2]. However, these comprehensive approaches incur substantial computational costs that limit their practical application, principally through computer memory constraints and the requirement to invert large matrices with lower-upper (LU) factorisations.

To alleviate these demands, the slowly varying nature of convective disturbances in boundary layers has been exploited to devise radically more efficient parabolic-type streamwise-marching techniques. The parabolised stability equations (PSE) marked a significant breakthrough; the technique adopted a slowly varying shape function coupled with a rapidly varying modal wave ansatz, alongside an iteration procedure [3], loosely based on the formal WKB (Wentzel-Kramers-Brillouin) approach. However, the PSE formulation suffers from a key weakness: the numerical marching procedure is ill-posed that manifests as numerical instability if the streamwise numerical discretisation step-size (Δx) becomes small. In incompressible flows, a stable march requires $\Delta x > 1/\alpha$, with α the evolving disturbance streamwise wavenumber. This step-size restriction must be enforced with implicit marching [4, 5]. When it becomes overly restrictive, one may circumvent it via regularisation: adding artificial damping to permit smaller steps [6], or neglecting the streamwise disturbance pressure gradient $\partial p/\partial x$ in subsonic regions [7]. Each approach introduces characteristic errors: implicit Euler and damping methods corrupt the wave ansatz with spurious wavelengths and growth rates, whilst pressure-gradient relaxation attenuates acoustic waves and corrupts both the wave ansatz and shape function; see Towne et al. [8] for a comprehensive critique. Furthermore, PSE suffers from fundamental limitations in receptivity modelling [9]. Near the leading edge, streamwise and wall-normal disturbance developments occur over comparable length scales, violating the slowly-varying flow assumption essential to PSE validity. Consequently, PSE cannot resolve the rapid spatial evolution characteristic of this critical region.

To overcome these limitations, the One-Way Navier-Stokes (OWNS) method was proposed. The technique can be made fully stable numerically: there is no imposed minimum step-size restriction and crucially the streamwise pressure gradient $\partial p/\partial x$ is retained in the governing equations. The approach relies on the assumption that downstream and upstream dynamics evolve independently, permitting their mathematical separation; a considerably less restrictive condition than the slowly varying assumption underpinning PSE. Originally applied to the Euler equations [10, 11], OWNS was later extended to general hyperbolic systems [12] and further adapted for compressible boundary layer flows [13]. The method is generally regarded to be more mathematically and physically sound, as opposed to the “ad-hoc” or “engineering” label ascribed to the PSE approach. The latest advancement, OWNS-Recursion (OWNS-R), leverages an efficiently constructed projection operator that, when applied to the state vector, selectively filters out upstream-propagating waves while preserving downstream components [14].

Relative to the simplicity of the PSE model, OWNS-R has superior physical fidelity, though it incurs substantially greater computational expense and requires considerable expertise in prescribing an effective OWNS recursion stabilisation procedure. PSE codes operate with minimal user intervention, requiring little manual calibration. Conversely, each flow configuration within the OWNS framework necessitates careful analysis and determination of specific

flow-dependent recursion parameters through continuous tracking of discrete and continuous spectra as the background flow evolves. The recursion parameters are thus critical to both the accuracy and numerical stability of the method: imprecise placement within the complex plane induces slow convergence and necessitates a trial-and-error calibration for each baseflow configuration under investigation. Critically, incorrect parameter selection leads to numerical instability. Recognising this fundamental limitation, Sleeman and Colonius [15] examined the merits of multiple OWNS-type techniques, including OWNS-R, and proposed a greedy algorithm to enhance robustness and automation of recursion parameter selection. Their algorithm initialises with user-specified parameter sets derived from pre-analysis of Euler-driven uniform flows, combined with randomly selected recursion parameters, to determine an optimal configuration satisfying prescribed objective functions.

Whilst the machine-learning/greedy-algorithmic approach of Sleeman and Colonius [15] offers a potential pathway towards automation, we contend that a fundamental understanding of how continuous spectra evolve under varying flow conditions (Reynolds number, frequency, and wavenumbers) provides the mathematical foundation for truly robust methodologies. This becomes particularly critical in transonic airflows, where the external inviscid flow accelerates from subsonic attachment points to supersonic conditions around aerofoil surfaces. Moreover, in hypersonic or swept-wing configurations, eigenvalues and continuous spectra occupy distinct complex plane regions that evolve dramatically with varying external flow speeds. Such radical spectral migration suggests that greedy algorithms, whilst promising, require substantial augmentation when confronting genuinely novel flow regimes or parameter spaces. Consequently, the use of OWNS over PSE would thus only be warranted where the step-size restriction of PSE proves limiting, or when modelling non-modal phenomena. In cases where these constraints are absent, PSE remains the preferred method, having demonstrated excellent agreement with DNS and LHNS models in numerous detailed investigations [16, 17].

Badcock and Mughal [18] applied the OWNS-R framework to investigate disturbance propagation through boundary layers containing laminar separation bubbles (LSBs), revealing fundamental limitations. Crucially, they demonstrated that whilst OWNS-R fails when marching through the LSB with the requisite small step-sizes, PSE maintains stability under identical conditions. This contrasting behaviour between the two spatial marching techniques warrants careful examination. OWNS-R demands exceptionally small streamwise step-sizes for accurate resolution of disturbance amplitudes. However, it was found that the LSB induces numerical instabilities precisely when small step-sizes commensurate with the bubble extent are employed. These numerical instabilities manifest through two mechanisms. First, elliptic effects associated with flow reversal compromise the one-way propagation assumption. Second, complex flow topology can disrupt the recursion parameter selection algorithm essential to OWNS-R stability. Thus, while PSE's modal formulation accommodates the complex flow physics within LSBs at larger step-sizes, the non-modal OWNS-R framework cannot simultaneously satisfy accuracy and stability requirements.

The limitations of OWNS manifest in two critical ways. First, selecting and placing recursion parameters remains challenging and does not generalize well across different flow configurations, making the method impractical for routine engineering use. Second, the inherently stiff nature of disturbance evolution requires exceptionally fine streamwise discretization, creating substantial computational costs.

The present paper addresses these limitations through two principal contributions. First, we develop a novel modal-OWNS (M-OWNS) methodology that synthesises the computational efficiency and operational simplicity of modal PSE with the enhanced numerical robustness of the OWNS recursion-stabilised procedure, whilst retaining the crucial $\partial p/\partial x$ pressure term. This hybrid approach demonstrates the capacity to model both modal and non-modal phenomena with substantially reduced computational overhead compared to standard OWNS, providing a more accessible framework for practical engineering applications. Second, we undertake a systematic investigation of recursion parameter selection and its automation, particularly for flows undergoing significant spectral evolution, through detailed analysis of continuous spectral curves in the complex plane.

The structure of the paper is thus as follows. In §2, the governing equations are introduced and we briefly review the background to the OWNS-R procedure. The methodology designed to address numerical aspects of the modal-OWNS is subsequently described in §3, where we demonstrate that the OWNS-R projection operator can be utilised to parabolise the modal form of the LHNS operator. Validation and efficacy of the proposed M-OWNS are undertaken in §4 through systematic investigation of flows with increasing complexity. In §4.2, we examine Tollmien-Schlichting (T-S) disturbances propagating in compressible flat-plate boundary layers across a range of Mach numbers from incompressible to $M = 0.8$, demonstrating the method's robustness throughout the subsonic regime. We subsequently analyse an incompressible swept cylinder Hiemenz boundary layer flow with curvature terms in §4.3, showcasing the technique's capability to handle curved geometry and crossflow (CF) disturbances. Finally, in §4.4, we investigate supersonic flow at $M = 4.5$ under various initialisation conditions, examining the method's performance in capturing disturbances originating from eigenfunction forcing, forcing with freestream acoustic waves, and direct mode excitation using suction and blowing at the wall.

2 Modal and Non-Modal Stability Equations

We consider the body-fitted compressible Navier-Stokes equations summarised in Appendix A. The goal of the work is to eventually model disturbance evolution in three-dimensional boundary layers, typically arising on *infinite* swept aircraft wings. The boundary layer is thus based on the assumption that the velocity, pressure, and temperature fields are invariant in the spanwise (z) direction.

See Zhu and Towne [14] for technical details of the OWNS-R approach. In this paper, we confine our discussion to those aspects of the OWNS-R approach requiring modification for the modal formulation.

2.1 Two-way Disturbance Evolution Equation

The governing Eqs. (A2)–(A8) can be written as the 5×5 system

$$\frac{\partial \bar{q}}{\partial t} = \mathcal{N} \bar{q}, \quad (1)$$

where \mathcal{N} is the non-linear Navier-Stokes operator, and $\bar{q} = (\bar{p}, \bar{u}, \bar{v}, \bar{w}, \bar{T})^T$ is the state vector. We then decompose the state vector into Q , a known invariant in z and time-independent

baseflow, and q , a small harmonic disturbance with frequency ω and a spanwise Fourier mode of wavenumber β in z ,

$$\bar{q}(x, y, z, t) = Q(x, y) + q(x, y) \exp(i\beta z - i\omega t). \quad (2)$$

Substituting this ansatz into Eq. (1) and then linearising with respect to q yields the LHNS, which can be expressed as

$$A \left(\frac{\partial}{\partial y} ; \beta \right) \frac{\partial q}{\partial x} = B \left(\frac{\partial}{\partial y} ; \beta, \omega \right) q + C \frac{\partial^2 q}{\partial^2 x}. \quad (3)$$

Here, A , B and C represent linear operators. The steady baseflow $Q(x, y)$ and its derivatives are obtained from a standard boundary layer solver (see, Mughal [19]). For linear disturbances, the C operator may be omitted without loss of accuracy [20], but analysis can be conducted with its retention too.

After discretising in the wall-normal direction, the spatial evolution equation takes the semi-discrete form

$$\mathbf{A} \frac{\partial \phi}{\partial x} = \mathbf{B} \phi, \quad (4)$$

where \mathbf{A} is typically singular for boundary-layer flows, reflecting the presence of algebraic (non-propagating) constraints alongside propagating dynamics. To analyse the evolution, we seek a modal decomposition based on the generalised eigenvalue problem

$$a_k \mathbf{A} \phi_k = i b_k \mathbf{B} \phi_k, \quad (5)$$

where ϕ_k are the right eigenvectors and $a_k, b_k \in \mathbb{C}$ with $b_k \neq 0$. When $a_k \neq 0$, the eigenvalue exists and we define

$$i\lambda_k = i \frac{b_k}{a_k}. \quad (6)$$

Because \mathbf{A} may be singular, the standard eigendecomposition must be generalised through a biorthogonal set of left and right eigenvectors. The left eigenvectors ψ_k satisfy

$$a_k \psi_k^* \mathbf{A} = i b_k \psi_k^* \mathbf{B}. \quad (7)$$

We normalise the eigenvectors such that the pairs (ψ_j, ϕ_k) satisfy the biorthogonality conditions:

$$\psi_j^* \mathbf{A} \phi_k = \delta_{jk}, \quad \psi_j^* \mathbf{B} \phi_k = \delta_{jk} i\lambda_k, \quad (8)$$

where $\lambda_k = b_k/a_k$ for modes with $a_k \neq 0$. Collecting right eigenvectors into \mathbf{V} and left eigenvectors into Ψ , and defining $\mathbf{U} = \Psi^* \mathbf{A}$, these relations give

$$\mathbf{U} \mathbf{V} = \Psi^* \mathbf{A} \mathbf{V} = \mathbb{I}, \quad \mathbf{V} \mathbf{U} = \mathbf{V} \Psi^* \mathbf{A} = \mathbb{I}, \quad \Psi^* \mathbf{B} \mathbf{V} = i\Delta, \quad (9)$$

where \mathbb{I} is the identity restricted to the finite-eigenvalue subspace, and $i\Delta = \text{diag}(i\lambda_k)$ for those modes with $a_k \neq 0$.

This biorthogonal basis allows the spatial generator of the dynamics to be expressed in modal form without inverting \mathbf{A} . Defining the modal operator \mathbf{M} via

$$\frac{\partial \phi}{\partial x} = \mathbf{M}\phi, \quad (10)$$

we obtain the compact decomposition

$$\mathbf{M} = \mathbf{V} i\Delta \mathbf{U}. \quad (11)$$

When \mathbf{A} is invertible, $\mathbf{U} = \mathbf{V}^{-1}$ and this reduces to the standard eigendecomposition. In practice, however, \mathbf{M} is never formed explicitly; instead, numerical methods work directly with the generalised problem, enabling a stable and physically meaningful representation even when \mathbf{A} is singular.

2.2 Modal and Non-Modal Disturbances

In the context of solving Eq. (10), it is crucial to distinguish between two types of solutions; *modal* and *non-modal*. We expand ϕ in terms of the eigenfunctions of \mathbf{M} , ϕ_k

$$\phi(x) = \sum_k c_k(x)\phi_k(x), \quad (12)$$

where the scalar c_k is an expansion coefficient. Thus a modal disturbance, ϕ_M , can be represented by a single, often the most dominant, eigenfunction of \mathbf{M} . These solutions encompass well-established fluid dynamic phenomena, including T-S and CF disturbances. In this case, there exists a particular eigenfunction ϕ_k of \mathbf{M} such that $\phi_M(x) = \phi_k(x)$. Multimodal or non-modal disturbances, ϕ_{NM} , arise as a linear combination of multiple eigenfunctions of \mathbf{M} . The spatial evolution of these disturbances cannot be captured by a single modal representation, but with a linear superposition of eigenfunctions given by Eq. (12).

Over large spatial distances, in a low disturbance environment, the behaviour of non-modal disturbances is always modal; most flows have only one or two growing eigenfunctions and these dominate over large distances. Over shorter distances however, non-modal disturbances can show significant transient growth with the linear combination of decaying eigenfunctions interacting in complex ways [21]. The solution is highly dependent on the streamwise initialising inflow state. Despite this, in the non-modal expansion there may be one dominant eigenfunction, the modal solution, that interacts weakly with the remaining decaying eigenfunctions. In such cases these disturbances can be called weakly non-modal.

2.2.1 Disturbance Energy

Quantifying disturbance growth requires an appropriate energy measure. Following established practice [22, 23], we define an inner product between disturbances ϕ_1 and ϕ_2 as

$$(\phi_1, \phi_2)_{\mathcal{H}} = \int_0^{\infty} \phi_1^* \mathcal{H} \phi_2 dy, \quad (13)$$

where \mathcal{H} is a positive definite Hermitian matrix. For our analysis, we adopt the density-weighted kinetic energy norm [24, 25], which emphasises the momentum components of the disturbance:

$$\mathcal{H} = \text{diag} (0, \bar{\rho}, \bar{\rho}, \bar{\rho}, 0), \quad (14)$$

$$E_{\mathcal{H}} = \frac{1}{2} \int_0^\infty \bar{\rho} (|u|^2 + |v|^2 + |w|^2) dy, \quad (15)$$

where $\bar{\rho}$ is the baseflow density.

2.2.2 Wavenumber Extraction

Let $\phi(x, y)$ be a solution to Eq. (4). We extract the complex wavenumber $\alpha(x)$ through the relation

$$\alpha = -i \frac{(\phi, \partial_x \phi)_{\mathcal{H}}}{\|\phi\|_{\mathcal{H}}^2}, \quad (16)$$

where ∂_x represents streamwise differentiation and $\|\phi\|_{\mathcal{H}}^2 = (\phi, \phi)_{\mathcal{H}}$. This definition naturally emerges from considering modal disturbances of the form $\phi_k \propto \exp(i\lambda_k x)$, where the wavenumber extraction recovers $\alpha = \lambda_k$ precisely. However, the expression applies universally to both modal and non-modal disturbances, yielding distinct physical interpretations.

Modal disturbances:

For a disturbance dominated by a single eigenfunction, $\phi = c_k(x)\phi_k(x)$, the extracted wavenumber from Eq. (16) approximates the generalised eigenvalue λ_k when the coefficient $c_k(x)$ varies sufficiently slowly relative to the eigenfunction's spatial scale. In the limit of parallel flow, where \mathbf{M} remains constant and c_k is genuinely constant, Eq. (16) yields $\alpha = \lambda_k$ precisely, ensuring $i\alpha \in \sigma(\mathbf{M})$.

For weakly non-parallel flows, the slowly-varying approximation permits $c_k(x)$ to evolve on spatial scales much longer than the characteristic wavelength, such that $|dc_k/dx| \ll |c_k \lambda_k|$. Under this condition, the wavenumber extraction remains approximately equal to λ_k . This quasi-modal regime preserves the essential character of single-eigenfunction solutions whilst acknowledging the gradual adaptation of the coefficient to the evolving baseflow. The approximation fails in regions of rapid baseflow variation, where the scale separation hypothesis breaks down and inter-modal coupling becomes significant.

Non-modal disturbances:

For multimodal disturbances expanded as in Eq. (12), the wavenumber becomes

$$\alpha = -i \frac{\sum_j \sum_k c_j [\partial_x c_k (\phi_j, \phi_k)_{\mathcal{H}} + c_k (\phi_j, \partial_x \phi_k)_{\mathcal{H}}]}{\sum_j \sum_k c_j c_k (\phi_j, \phi_k)_{\mathcal{H}}}. \quad (17)$$

This represents a weighted average of modal wavenumbers, with weights determined by the instantaneous energy distribution amongst modes. The cross terms $(\phi_j, \partial_x \phi_k)_{\mathcal{H}}$ introduce additional phase variations arising from inter-modal interactions. Unlike modal wavenumbers belonging to $\sigma(\mathbf{M})$, this composite quantity varies with the disturbance composition $c_k(x)$ and provides a local measure of phase velocity and amplification.

2.3 Modal Formulation

Suppose we seek solutions of Eq. (4) of the form

$$\phi(x) = \tilde{\phi}(x) \exp i\Theta(x) \quad (18)$$

where $\Theta_x = \alpha$. We call Eq. (18) the modal decomposition of ϕ . Under this decomposition the two-way semi-discrete Eq. (4), transforms into the modal two-way equation

$$\tilde{\mathbf{A}} \frac{\partial \tilde{\phi}}{\partial x} = \tilde{\mathbf{B}} \tilde{\phi}, \quad (19)$$

where the modal operators $\tilde{\mathbf{A}}$ and $\tilde{\mathbf{B}}$ are given by $\tilde{\mathbf{A}} = \mathbf{A}$, and $\tilde{\mathbf{B}} = \mathbf{B} - i\alpha \mathbf{A}$. Importantly, we retain the pressure derivative $\partial p/\partial x = i\alpha \tilde{p} + \partial \tilde{p}/\partial x$ in its entirety in what follows; in conventional PSE the $\partial \tilde{p}/\partial x$ term is generally set to zero in subsonic regions.

Given an eigenfunction-eigenvalue pair of Eq. (5), ϕ_k and λ_k , it follows that the corresponding $\tilde{\phi}_k$ satisfies the GEVP

$$i(\lambda_k - \alpha) \tilde{\mathbf{A}} \tilde{\phi}_k = \tilde{\mathbf{B}} \tilde{\phi}_k. \quad (20)$$

The modal spatial marching operator, $\tilde{\mathbf{M}}$, can be found using the eigenfunctions of \mathbf{M} , defined by Eq. (9):

$$\tilde{\mathbf{M}} = \mathbf{V} i(\Delta - \alpha \mathbf{I}) \mathbf{U} = \mathbf{V} i\Delta \mathbf{U} - i\alpha \mathbf{V} \mathbf{U} = \mathbf{M} - i\alpha \mathbf{I}, \quad (21)$$

when restricted to the finite eigenspace of \mathbf{M} . This equation implies that \mathbf{M} and $\tilde{\mathbf{M}}$ share the same eigenfunctions and that the spectrum of the modal equation is identical to that of the non-modal equation, but shifted by $-i\alpha$. Thus, the finite spectrum of \mathbf{M} takes the form $\sigma(\tilde{\mathbf{M}}) = \{\lambda - \alpha : \lambda \in \sigma(\mathbf{M})\}$. The physical meaning of α depends on the initial conditions and disturbance being tracked. If the disturbance is modal then α is the eigenvalue of the wave, whereas if the disturbance is non-modal then α is the averaged wavenumber quantity described by Eq. (17).

Note that if \mathbf{C} is retained in Eq. (4), it yields the modal two-way equation

$$\tilde{\mathbf{A}} \frac{\partial \tilde{\phi}}{\partial x} = \tilde{\mathbf{B}} \tilde{\phi} + \tilde{\mathbf{C}} \frac{\partial^2 \tilde{\phi}}{\partial x^2}, \quad (22)$$

where

$$\tilde{\mathbf{A}} = \mathbf{A} - 2i\alpha \mathbf{C}, \quad \tilde{\mathbf{B}} = \mathbf{B} - i\alpha \mathbf{A} + \left(i \frac{\partial \alpha}{\partial x} - \alpha^2 \right) \mathbf{C}, \quad \text{and} \quad \tilde{\mathbf{C}} = \mathbf{C}. \quad (23)$$

2.3.1 Adaptive Iteration Method

The modal formulation introduces an ambiguity through the phase function Θ , which requires determination. The adaptive iteration procedure resolves this by iteratively refining the wavenumber estimate to converge upon the wavenumber of the disturbance.

Consider a disturbance ϕ possessing a generalised wavenumber α at a particular streamwise location. Given an estimate α_k , Eq. (20) implies

$$\frac{\partial \tilde{\phi}}{\partial x} = i(\alpha - \alpha_k)\tilde{\phi}. \quad (24)$$

In a similar way to deriving Eq. (16), taking the inner product of this equation and rearranging gives

$$\alpha = \alpha_k - i \frac{(\tilde{\phi}_k \partial_x \tilde{\phi}_k)_{\mathcal{H}}}{\|\tilde{\phi}_k\|_{\mathcal{H}}^2}. \quad (25)$$

The adaptive iteration procedure uses this equation to generate a sequence $\{\alpha_k\}$ converging to α through

$$\alpha_{k+1} = \alpha_k - i \frac{(\tilde{\phi}_k \partial_x \tilde{\phi}_k)_{\mathcal{H}}}{\|\tilde{\phi}_k\|_{\mathcal{H}}^2}, \quad k = 0, 1, \dots, \quad (26)$$

where $(\alpha_k, \tilde{\phi}_k)$ solve Eq. (20).

This iterative scheme forms the basis of the PSE [7] and adaptive-LHNS [26, 27] methods. Convergence occurs when $|\alpha_{k+1} - \alpha_k| < \mathcal{E}$ for prescribed tolerance \mathcal{E} , typically requiring 3-5 iterations for $\mathcal{E} = 10^{-9}$.

2.3.2 Validity of the Modal Approach

The modal ansatz (18) requires that the decomposition accurately represents the underlying disturbance field. The normalised modal error arising from the iteration satisfies

$$\epsilon = \frac{|\Delta \tilde{\phi}|}{|\tilde{\phi}|} + \Delta x |\alpha - \alpha_k| \ll 1, \quad (27)$$

where $\Delta \tilde{\phi}$ denotes the shape function variation over the streamwise increment Δx , and α_k represents the wavenumber at iteration k .

Crucially, whilst the iteration procedure can, in principle, drive the second term to negligible values for any step-size through convergence of $\alpha_k \rightarrow \alpha$, the first term remains fixed by the underlying physics. The ratio $|\Delta \tilde{\phi}|/|\tilde{\phi}|$ depends solely on the disturbance structure and the chosen Δx – iteration cannot reduce this contribution. Therefore, the validity of the modal approach reduces to the requirement that for a given streamwise step Δx and converged wavenumber α , the shape function variation satisfies :

$$\frac{|\Delta \tilde{\phi}|}{|\tilde{\phi}|} \sim 0. \quad (28)$$

This criterion delineates three regimes:

1. **Slowly varying regime:** The shape function varies sufficiently slowly that (28) holds for step-sizes substantially larger than those required by non-modal methods. The disturbance field admits efficient modal representation, typically when a single eigenfunction dominates and $\tilde{\phi}$ captures only amplitude modulation.

2. **Moderately varying regime:** Moderate step-sizes satisfy (28). The modal approach remains advantageous but with diminished computational savings. This occurs when multiple modes contribute but retain some coherent structure that the modal ansatz partially captures.
3. **Rapidly varying regime:** Only step-sizes comparable to non-modal requirements satisfy (28). The shape function varies as rapidly as the phase itself, indicating broadband spectral content or strong modal interactions that resist efficient modal decomposition.

The transition between regimes manifests naturally through the step-size required to satisfy (28). As the flow evolves from quasi-parallel conditions (favouring modal behaviour) toward regions of strong non-parallelism or modal interaction, progressively smaller values of Δx becomes necessary to maintain validity of the modal ansatz.

Crucially, the modal formulation retains numerical stability across all disturbance types, without invoking the parallel flow or quasi-parallel flow hypothesis. Provided $\tilde{\phi}$ and $\partial\tilde{\phi}/\partial x$ exist and are continuous throughout the marching domain, as $\Delta x \rightarrow 0$, $\varepsilon \rightarrow 0$ irrespective of modal content, ensuring convergence for arbitrary initial conditions. This robustness permits systematic application to both modal and non-modal disturbances, with computational efficiency determined by the inherent scale separation within the disturbance field.

2.4 Initialisation of the Spatial March

For the spatial march, we may initiate either modal or non-modal disturbances. To enable the modal disturbance, we prescribe a locally parallel eigenfunction of the operator \mathbf{M} as the inflow state. The streamwise-marching procedure then computes the spatial evolution of this eigenfunction under the action of the parabolised \mathbf{M} operator. However, the solution need not remain modal throughout the march; since \mathbf{M} contains all its one-way eigenfunctions, the evolving solution admits multimodal phenomena. In supersonic flows, this is exemplified by the spontaneous generation of sound that occurs from the creation of Mack's second mode [28].

Non-modal initialisation may use linear combinations of locally parallel eigenfunctions of \mathbf{M} , random noise, freestream waves, or wall suction/blowing; these techniques are commonly utilised in optimal disturbance analysis [29]. Such solutions exhibit transient growth over short streamwise distances from the inflow plane; on decay of transients, the solution generally evolves or is attracted towards the modal structure. Hence, the distinction between modal and non-modal evolution is not absolute in the spatial marching framework.

3 OWNS-R and M-OWNS

Equation (4) represents a two-way evolution equation, where the semi-discrete operator \mathbf{M} accommodates eigenfunctions that propagate in both downstream and upstream directions. Through the application of Briggs' criteria [30], we can identify the corresponding eigenvalues of these propagating modes. Alternatively, we can examine the sign of the group velocity as a first-order approximation to the Briggs' criteria. Consequently, the finite spectrum of \mathbf{M} can

be partitioned into three distinct subsets :

$$\sigma(\mathbf{M}) = \begin{cases} \text{downstream-propagating eigenvalues} \\ \text{upstream-propagating eigenvalues} \\ \text{zero eigenvalues.} \end{cases} \quad (29)$$

The zero eigenvalues correspond to stationary modes that exhibit no propagation upstream or downstream. The equation in its current form presents challenges for stable downstream marching; namely the wavelength of the downstream-propagating modes of interest exists on a scale comparable to that of elliptical acoustic waves [4], which propagate bidirectionally. During the spatial march, the integrator erroneously interprets upstream-decaying acoustic waves as downstream-growing waves, resulting in numerical instabilities [8].

Instead of simply stepping over the upstream-propagating waves, we seek to completely remove the influence of the upstream-propagating waves from \mathbf{M} in a computationally efficient way. In other words, we wish to create a one-way or parabolised operator \mathbf{M}^+ , with a finite spectrum that can be decomposed into

$$\sigma(\mathbf{M}^+) = \begin{cases} \text{downstream-propagating eigenvalues} \\ \text{zero eigenvalues.} \end{cases} \quad (30)$$

We call \mathbf{M}^+ parabolised if it satisfies Eq. (30), and denote $\sigma(\mathbf{M}^+)$ the corresponding set of downstream-propagating eigenvalues. Similarly, we define \mathbf{M}^- as the complementary upstream operator of \mathbf{M} with $\sigma(\mathbf{M}^-)$ the set of upstream-propagating eigenvalues.

3.1 The Projection Operator

As discussed by Towne [31] and Towne et al. [32], one valid method of turning \mathbf{M} into a one-way operator is with the creation of a projection operator \mathbf{P} such that

$$\mathbf{M}^+ = \mathbf{PM}. \quad (31)$$

The role of \mathbf{P} is to turn off all of the upstream-propagating eigenvalues of \mathbf{M} . Proposed by Towne [31], with the infinite dimensional theory developed by Rudel et al. [33] with pseudo-differential operators, one form of \mathbf{P} can be found by considering the eigenvalue decomposition of $\mathbf{M} = \mathbf{Vi}\Delta\mathbf{U}$ given by Eq. (11) :

$$\mathbf{P} = \mathbf{VEU}, \quad (32)$$

for the finite eigenvalues of \mathbf{M} only. Here, \mathbf{E} is the diagonal matrix constructed only out of ones and zeros in such a way the j th entry of the matrix $\mathbf{E}\Delta$ has the property

$$(\mathbf{E})_j = \begin{cases} 1 & \text{if } (\Delta)_j \text{ is downstream-propagating,} \\ 0 & \text{otherwise.} \end{cases} \quad (33)$$

Thus, we have

$$(\mathbf{E}\Delta)_j = \begin{cases} (\Delta)_j & \text{if } (i\Delta)_j \text{ is downstream-propagating,} \\ 0 & \text{otherwise.} \end{cases} \quad (34)$$

The operator \mathbf{M}^+ then has the form

$$\mathbf{M}^+ = \mathbf{P}\mathbf{M} = \mathbf{V}i\mathbf{E}\Delta\mathbf{U}, \quad (35)$$

and its spectrum satisfies Eq. (30). It is also clear that \mathbf{P} and \mathbf{M} commute

$$\mathbf{PM} = \mathbf{V}i\mathbf{E}\Delta\mathbf{U} = \mathbf{V}i\Delta\mathbf{E}\mathbf{U} = \mathbf{MP}, \quad (36)$$

since \mathbf{E} and Δ are diagonal matrices. It is also easy to show that $\mathbf{M}^- = (\mathbb{I} - \mathbf{P})\mathbf{M}$ from the definition Eq. (34).

3.2 One-Way Projection Operator for Modal Disturbances

We now show that the projection operator \mathbf{P} parabolises the modal operator $\tilde{\mathbf{M}}$ – provided it parabolises the operator \mathbf{M} .

If $\mathbf{P} = \mathbf{V}\mathbf{E}\mathbf{U}$ parabolises \mathbf{M} then \mathbf{E} must satisfy the identity Eq. (33). Expanding the modal operator $\tilde{\mathbf{M}}$ in terms of the eigendecomposition of \mathbf{M} from Eq. (20) yields

$$\tilde{\mathbf{M}} = \mathbf{V}(i\Delta - i\alpha\mathbb{I})\mathbf{U}. \quad (37)$$

Applying \mathbf{P} to the left-hand-side of $\tilde{\mathbf{M}}$ results in

$$\mathbf{P}\tilde{\mathbf{M}} = \mathbf{PV}(i\Delta - i\alpha\mathbb{I})\mathbf{U} = \mathbf{VEV}^{-1}\mathbf{V}(i\Delta - i\alpha\mathbb{I})\mathbf{U} = \mathbf{ViE}(\Delta - \alpha)\mathbf{U}. \quad (38)$$

From Eqs. (33) and (34) it is clear that the operator $\mathbf{E}(\Delta - \alpha)$ has the property

$$[\mathbf{E}(\Delta - \alpha)]_j = \begin{cases} [\mathbf{E}(\Delta - \alpha)]_j & \text{if } (\Delta)_j \text{ is downstream-propagating,} \\ 0 & \text{otherwise.} \end{cases} \quad (39)$$

Therefore, the operator $\tilde{\mathbf{M}}^+ = \mathbf{P}\tilde{\mathbf{M}}$ is a one-way operator.

3.3 The Approximate Projection Operator: OWNS-R

Next, we briefly summarise the construction of the projection operator, devised by Zhu and Towne [14], which recursively filters the upstream-propagating eigenvalues out of the spectrum of \mathbf{M} . Following this, we then describe how this procedure is modified for the modal form of the equations.

The eigenvalue decomposition in the projection operator \mathbf{P} , Eq. (32), is very expensive to evaluate explicitly at each spatial marching step. Instead, Zhu and Towne [14] proposed the OWNS-R technique which aims to achieve a stable streamwise-march more efficiently with an

approximate form of \mathbf{P} . The projection operator \mathbf{P} is approximated via a operator \mathbf{P}_{N_β} . This *approximate*-projection operator is dependent on a sequence of complex recursion parameters

$$\beta^\pm = (\beta_k^+, \beta_k^-)_{j=1, \dots, N_\beta} \subset \mathbb{C}^2, \quad N_\beta \in \mathbb{N}. \quad (40)$$

The sets β^+ and β^- are called the positive and negative recursion parameters respectively. We require this approximation to satisfy $\lim_{N_\beta \rightarrow \infty} \mathbf{P}_{N_\beta} = \mathbf{P}$, with appropriately placed β^\pm . One possible form of the approximate projection operator is

$$\mathbf{P}_{N_\beta} = \left(\mathbb{I} + c \prod_{k=1}^{N_\beta} (\mathbf{M} - i\beta_k^+ \mathbb{I}) (\mathbf{M} - i\beta_k^- \mathbb{I})^{-1} \right)^{-1}, \quad (41)$$

where $c > 0$ is a tuning parameter [14]. Small c helps retain spectra near β^+ and large c helps remove spectra near β^- .

Instead of explicitly calculating the operator \mathbf{M}^+ and solving the one-way equation

$$\frac{\partial \phi}{\partial x} = \mathbf{M}^+ \phi = \mathbf{P}_{N_\beta} \mathbf{M} \phi, \quad (42)$$

we solve ϕ directly from the two-way equation

$$\frac{\partial \phi}{\partial x} = \mathbf{M} \phi, \quad (43)$$

and calculate the approximate projected state vector as $\phi^+ = \mathbf{P}_{N_\beta} \phi$. This prevents the need to construct \mathbf{P}_{N_β} . This is a consequence of the \mathbf{P} and \mathbf{M} commuting.

To evaluate the action of \mathbf{P}_{N_β} on the state vector, we factorise the operator in a way that allows it to be calculated recursively. See Zhu and Towne [14] for more details. The form of \mathbf{P}_{N_β} is then

$$\mathbf{P}_{N_\beta} = \frac{1}{c+1} \prod_{k=1}^{N_\beta} (\mathbf{M} - \mathbb{I} i\beta_k^*)^{-1} (\mathbf{M} - i\beta_k^- \mathbb{I}), \quad (44)$$

where $\beta_j^* \in \mathbb{C}$ are the solutions to the N_β -th order polynomial in α

$$c \prod_{k=1}^{N_\beta} (\alpha - \beta_k^+) + \prod_{k=1}^{N_\beta} (\alpha - \beta_k^-) = (c+1) \prod_{k=1}^{N_\beta} (\alpha - \beta_k^*). \quad (45)$$

This allows for the recursive computation of $\mathbf{P}_{N_\beta} \phi$, which is described next.

3.4 Modal and Non-modal OWNS Methodology

We now outline the computational steps in the full modal-OWNS and non-modal approaches. For numerical expediency, we never explicitly calculate \mathbf{M} , \mathbf{M}^+ or \mathbf{P}_{N_β} , but instead solve

every equation expressed in terms of \mathbf{A} and \mathbf{B} – reducing the computational overhead significantly. Thus, Eq. (44) should be written in the form

$$\mathbf{P}_{N_\beta} = \frac{1}{c+1} \prod_{k=1}^{N_\beta} (\mathbf{B} - i\beta_k^* \mathbf{A})^{-1} (\mathbf{B} - i\beta_k^- \mathbf{A}). \quad (46)$$

The steps are as follows:

1. Calculate ϕ implicitly from the non-modal two-way evolution Eq. (4), or $\tilde{\phi}$ from the modal two-way evolution Eq. (19) and the modal ansatz (18).
2. Calculate the streamwise wavenumber from the kinetic energy norm, using adaptive iteration when utilising the modal formulation
3. Calculate the projection of \mathbf{P}_{N_β} on ϕ (or $\tilde{\phi}$ for the modal formulation) : $\phi^+ = \mathbf{P}_{N_\beta} \phi$, using the recursions

$$\phi_0 = \frac{1}{c+1} \phi, \quad (47)$$

$$(\mathbf{B} - \mathbf{A} \beta_k^*) \phi_k = (\mathbf{B} - \mathbf{A} \beta_k^-) \phi_{k-1}, \quad k = 1, \dots, N_\beta, \quad (48)$$

$$\phi^+ = \phi_{N_\beta}. \quad (49)$$

We stress that this only works for a correct selection of recursion parameters β^\pm and c ; the parameters being specific to the particular flow studied (see §4.1).

4 Numerics, Recursion Parameters and Validation

The stability calculations are performed using an in-house compressible, spatial marching code that incorporates LST and PSE [19]. The OWNS results reported in this paper are from an entirely new and independently developed OWNS-R and M-OWNS solver.

Spatial discretisation in the wall-normal domain is achieved with fourth-order accurate finite differences with a stretched grid of Malik [25] given by

$$y_{\text{Malik}}(\eta, y_{\text{max}}, y_{\text{half}}) = \frac{a\eta}{b - \eta}, \quad (50)$$

where $0 \leq \eta \leq 1$ is the mapped uniform computational domain, and y_{max} is the truncation point of the far-field. More than half of the grid points are located between 0 and y_{half} (boundary layer), with

$$a = \frac{y_{\text{max}} y_{\text{half}}}{y_{\text{max}} - 2y_{\text{half}}}, \quad \text{and} \quad b = 1 + \frac{a}{y_{\text{max}}}. \quad (51)$$

The dimensional streamwise \bar{x} -direction employs second-order accurate backward differencing (BFD2) with Δx the step-size defined over $0 < \bar{x} < L_{\bar{x}}$, and n_x discretised points. The dimensional wall-normal domain is defined as $0 < \bar{y} < L_{\bar{y}}$, with n_y grid points. We let R_δ be the Reynolds number based on the local boundary layer thickness where $R_\delta = \sqrt{\bar{x}} R_\infty$, where R_∞ is the freestream Reynolds number and \bar{x} is the distance from the origin. All spatial quantities are non-dimensionalised with δ_0 , the boundary layer thickness at the initial streamwise location or inlet \bar{x}_0 . The temporal frequency and spanwise wavenumbers may be

non-dimensionalised as $F = \omega \times 10^6 / R$ and $b = \beta \times 10^3 / R$ respectively, where $R = R_\delta(\bar{x}_0)$ is the inlet Reynolds number. The baseflow is non-dimensionalised by freestream values at the inlet.

At the wall, boundary conditions include no-slip for velocity disturbances, and either a zero disturbance or adiabatic condition for temperature. In the freestream we use Thompson conditions to suppress numerical reflections [34]. For initial conditions, we either employ a locally parallel eigenfunction ϕ_{LST} obtained through LST, freestream waves, or excite disturbances using wall suction and blowing along the surface.

In the adaptive iteration process of M-OWNS and PSE, the error is calculated as the absolute value of the difference between the imaginary parts (*i.e.* growth rate) of successive wavenumbers. If the growth-rate is smaller than the overall error, we then switch to considering the absolute value of the difference. We denote the iteration error by \mathcal{E} and the number of iterations required to satisfy the error by N_{it} . The spectrum of the system at a particular streamwise location is computed using the QZ-algorithm.

4.1 Recursion Parameter Selection

The stability and accuracy of the OWNS spatial march depend critically upon the selection of complex recursion parameters β^\pm . These parameters must be chosen with reference to the spectral properties of the operator \mathbf{M} , with the selection strategy necessarily adapted to the specific flow configuration. We consider three canonical cases: two-dimensional subsonic flows, three-dimensional subsonic flows, and two-dimensional supersonic flows.

Following Towne and Colonius [12], the fundamental principle governing parameter selection requires positioning β^+ near downstream-propagating eigenvalues and β^- near upstream-propagating eigenvalues. To implement this strategy, we must first characterise the spectral structure of \mathbf{M} .

It is important to note that the operator \mathbf{M} in unbounded domains contains discretised representations of continuous spectra branches as well as the discrete isolated modes. Whilst the true continuous spectra are unbounded, due to the discretisation the numerical continuous spectra will be bounded and will become under resolved as we move away from the initial branch point.

The continuous spectrum can be determined analytically via frozen-coefficient analysis with freestream baseflow values. Substituting

$$\frac{\partial}{\partial x} \rightarrow i\alpha \quad \text{and} \quad \frac{\partial}{\partial y} \rightarrow i\eta, \quad (52)$$

into Eq. (3) yields the dispersion relation $\alpha = \Omega(\omega, \beta, \eta, M, R, U, W, T)$, where U_∞ and W_∞ denote the dimensional streamwise and spanwise freestream velocities and T_∞ the freestream temperature at each . In the linearised analysis, these are normalised by the local boundary layer edge velocity (U_e) and temperature (T_e) at the inlet, such that $U = U_\infty / U_e$ with $W = W_\infty / U_e$ representing the crossflow fraction, and $T = T_\infty / T_e$ is temperature.

Analysis of the dispersion relation in the incompressible viscous and compressible inviscid limits yields the continuous branch structure. These branches provide approximations to the

continuous spectra within $\sigma(\mathbf{M})$:

$$\alpha_{1,2,3}(\eta) = \frac{\omega - \beta W}{U} + \frac{i(\beta^2 + \eta^2)}{UR}, \quad \alpha_{4,5}(\eta) = \frac{M^2 U (\omega - \beta W) \pm \sqrt{\mu(\eta)}}{M^2 U^2 - T}, \quad (53)$$

where

$$\mu(\eta) = -\eta^2 (M^2 U^2 - T) + \beta^2 (M^2 T (U^2 + W^2) - T^2) - 2\beta M^2 T W \omega + M^2 T \omega^2. \quad (54)$$

The branches $\alpha_{1,2,3}$ represent the vorticity/entropy modes. These branches originate on the real axis and extend parallel to the imaginary axis as η^2 increases. The acoustic branches $\alpha_{4,5}$ exhibit qualitatively different behaviour [35], with the parameter $\mu(\eta)$ determining the acoustic branch structure. For $|\eta|$ sufficiently small, $\mu \geq 0$ and the acoustic branches remain purely real, representing evanescent waves. For $|\eta|$ sufficiently large, $\mu < 0$ and the branches acquire imaginary components, corresponding to propagating waves. When the spanwise wavenumber β exceeds a critical value in subsonic flows, the acoustic branches may appear entirely parallel to the imaginary axis without real components. These aspects are shown schematically in Fig. 1.

In subsonic flows, Briggs' criterion reveals that branches α_{1-4} propagate downstream whilst α_5 propagates upstream. In supersonic flows, all branches α_{1-5} propagate downstream, though upstream-propagating discrete acoustic modes exist, trapped beneath the sonic line [36]. Additionally, the spectrum of $\sigma(\mathbf{M})$ contains downstream-propagating discrete modes too.

Stable spatial marching requires eliminating the influence of α_5 whilst preserving α_{1-4} and all discrete modes. The critical spectral locations are given by:

$$d_1 = \frac{\omega - \beta W}{U}, \quad d_2 = \frac{M^2 U (\omega - \beta W)}{M^2 U^2 - T}, \quad d_{3,4} = \frac{M^2 U (\omega - \beta W) \pm \sqrt{\mu(0)}}{M^2 U^2 - T}, \quad (55)$$

where d_1 marks the endpoints of vorticity/entropy branches, d_2 the acoustic branch midpoint, and $d_{3,4}$ the propagating acoustic spectral endpoints. In subsonic flows, d_3 propagates downstream and d_4 upstream; both propagate downstream in supersonic flows.

The preceding analysis assumes locally parallel frozen flow. The actual spectral structure of \mathbf{M} may deviate from this, potentially compromising numerical stability in the OWNS-R formulation. Furthermore, the x -dependence of \mathbf{M} necessitates recalculating recursion parameters at each streamwise position, since the spectrum evolves as the local values of R , M and W vary.

To guide parameter selection, we employ the scalar projection operator

$$\mathcal{P}_{N_\beta}(z; \beta^\pm) = \left(1 + c \prod_{k=1}^{N_\beta} (z - i\beta_k^+) (z - i\beta_k^-)^{-1} \right)^{-1}, \quad (56)$$

obtained by replacing \mathbf{M} with $z \in \mathbb{C}$ in \mathbf{P}_{N_β} , Eq. (41). The magnitude $|\mathcal{P}_{N_\beta}(z; \beta^\pm)|$ indicates the filtering behaviour: values near unity preserve modes at z , whilst values near zero suppress them.

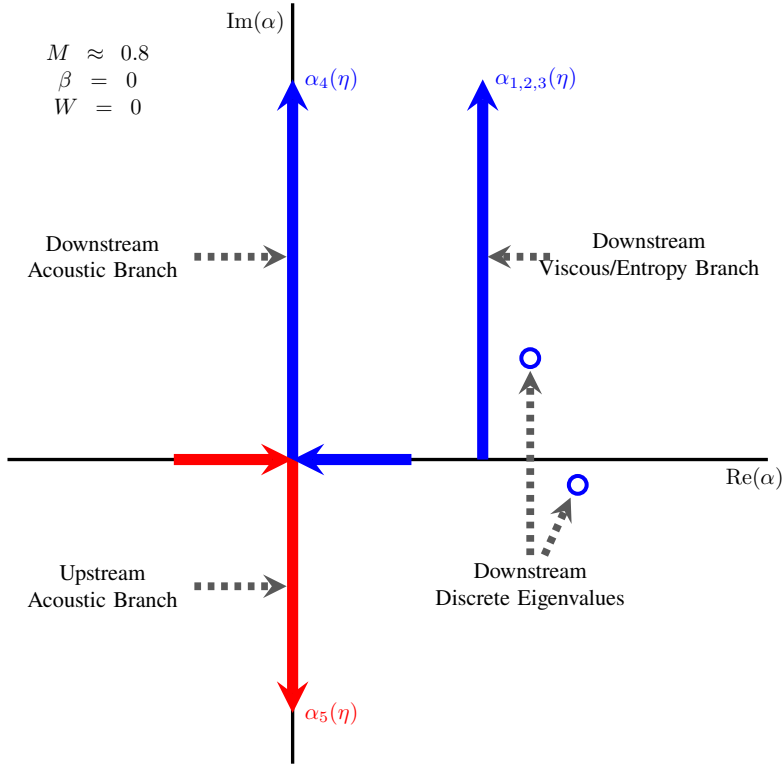


Fig. 1: Spectral structure of the streamwise spatial marching operator \mathbf{M} for compressible boundary layers under the parallel flow ($\beta = 0$, $W = 0$). The subsonic spectrum comprises continuous branches of downstream-propagating vorticity/entropy modes $\alpha_{1,2,3}(\eta)$ and acoustic mode $\alpha_4(\eta)$, an upstream-propagating acoustic branch $\alpha_5(\eta)$, and discrete eigenvalues (circles). Arrows denote the direction of increasing η^2 along each branch.

One constraint governs parameter selection: no β^- parameter may coincide with any element of $\sigma(M)$ to ensure invertibility of P_{N_β} . Additionally, Sleeman and Colonius [15] observe that parameters suitable for OWNS-R may prove incompatible with alternative OWNS formulations [12, 31], necessitating formulation-specific parameter determination.

4.2 Flat-Plate Subsonic Boundary Layers

We apply the M-OWNS technique to subsonic boundary layers over an isothermal flat-plate, describing the selection strategy and implementation of recursion parameters. The flow is characterised by freestream Reynolds number $R_\infty = 10^6 \text{ m}^{-1}$ and temperature $T_\infty = 298\text{K}$, with Mach numbers spanning $M = 0.02, 0.2, 0.5$ and 0.8 .

The computational domain is initialised at $R_\delta = 400$ using a locally parallel eigenfunction corresponding to the most unstable mode at the inlet. The analysis considers a non-dimensional frequency $F = 86$ and spanwise wavenumbers $b = 0, 0.1, 0.2$ and 0.3 . For this flat-plate

geometry, the metric term $\chi(x, y)$ given by Eq. (A1) reduces to unity with zero curvature $\kappa = 0$.

All subsonic calculations employ $n_y = 221$ discretised points in the wall-normal direction, with grid-stretching parameters $y_r = 600$ and $y_h = 10$.

4.2.1 Recursion Parameter Selection

For OWNS-R, precise determination of the complex recursion parameters β^\pm is essential and must be tailored to the specific flow under investigation. Our approach exploits the spectral structure of the operator \mathbf{M} , particularly the characteristic symmetry exhibited by subsonic flows. Specifically, the acoustic branches exhibit rotational symmetry about the point d_2 (Eq. (55)), which proves crucial for efficient parameter selection. By placing β^+ to capture downstream modes, we obtain β^- through rotation by π about d_2 , ensuring balanced treatment of the spectral branches.

We partition the N_β recursion parameters as follows:

$$N_v = \lceil N_\beta / 3 \rceil + 2, \quad N_a = N_\beta - N_v, \quad (57)$$

allocating N_v parameters to the vorticity/entropy branches and N_a to the acoustic branches. This non-uniform distribution proves crucial, with denser placement near the real axis where spectral filtering poses the greatest challenge.

The recursion parameters are computed as:

$$\beta_k^+ = \begin{cases} d_1 + i|\alpha_0|y_{\text{Malik}}\left(\frac{k-1}{N_v-3}, 1, 0.4\right) & \text{if } k = 1, \dots, N_v - 2 \\ \alpha_0 & \text{if } k = N_v - 1 \\ d_1 + 0.6(\alpha_0 - d_1) & \text{if } k = N_v \\ d_2 + i\alpha_{\max}y_{\text{Malik}}\left(\frac{k-N_v-1}{N_a-1}, 1, 0.12\right) + p & \text{if } k = N_v + 1, \dots, N_\beta \end{cases} \quad (58)$$

$$\beta_k^- = -(\beta_k^+ - d_2) + d_2, \quad (59)$$

where α_0 denotes the tracked discrete mode (or $|d_1|$ if absent), and y_{Malik} implements the non-uniform spacing defined in Eq. (50). The parameter $\alpha_{\max} = 28i$ bounds the acoustic branch extent, determined through systematic grid studies. The adjustment parameter

$$p = -5 \text{ sign}(d_1) \times 10^{-2} + 7.5i \times 10^{-3} \quad (60)$$

serves dual purposes: its imaginary component prevents singularities in \mathbf{P}_{N_β} by shifting β^- parameters away from the spectrum $\sigma(\mathbf{M})$, whilst the real component ensures robust parabolisation.

Figure 2 illustrates the placement of these recursion parameters for a flat-plate incompressible boundary layer ($M = 0.02$, $R = 400$, $F = 86$, $b = 0$), revealing inherent challenges in parameter selection. In incompressible two-dimensional flows, the downstream and upstream acoustic spectra form continuous lines that intersect near the origin. Numerical discretisation yields a discrete representation of these spectra, visible as the V-shaped acoustic branches in the figure, which deviate from the true analytic spectra.

This discrepancy creates significant complications for parameter selection. Recursion parameters placed near the intersection compete destructively: β^+ parameters attempt to capture upstream modes whilst β^- parameters simultaneously remove downstream modes. This difficulty intensifies for small ω values, where the vorticity/entropy branches migrate towards the acoustic spectra, causing recursion parameters on these branches to interfere with those targeting acoustic modes.

To address these challenges, we exploit the rotational symmetry of the spectra about d_2 . By treating the spectra as fully symmetric, we effectively construct fictitious upstream counterparts to the vorticity/entropy branches, thereby achieving balanced recursion parameter strengths around d_2 . This symmetry-based approach prevents any single parameter from dominating and ensures stable parabolisation even when spectral branches lie in close proximity.

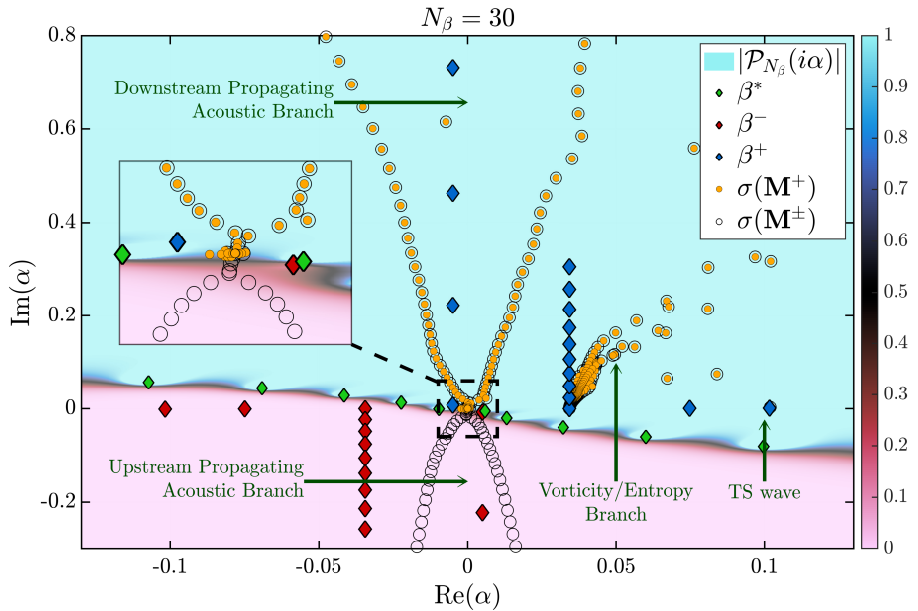


Fig. 2: Numerical spectrum of the two-way system $\sigma(\mathbf{M}^\pm) = \sigma(\mathbf{M})$ computed with the QZ method, and the parabolised downstream system $\sigma(\mathbf{M}^+) = \sigma(\mathbf{P}_{N_\beta} \mathbf{M})$ for a 2D boundary layer ($M = 0.02, R = 400, F = 86, b = 0, W = 0$) with $N_\beta = 30$. Downstream eigenvalues are preserved whilst upstream eigenvalues are eliminated. Blue and red diamonds represent β^+ and β^- recursion parameters, respectively. The green diamonds denote β^* parameters, roots of the characteristic polynomial and lie near the $|\mathcal{P}_{N_\beta}| = 0.5$ contour. The contours show the norm of \mathcal{P}_{N_β} , with teal regions (approximately 1) indicating retained modes and pink regions (approximately 0) indicating suppressed modes. Notable features include the acoustic and vorticity/entropy continuous branches, and the discrete T-S wave. The discrete T-S wave must be retained throughout the march, we place a recursion parameter on it as it evolves. In this case $c = 1$.

The adjustment parameter p further addresses these challenges by clamping the projection operator \mathcal{P}_{N_β} such that the contour $|\mathcal{P}_{N_\beta}| = 0.5$ passes through the origin parallel to the real axis, effectively separating the competing spectral regions. The figure confirms that all downstream-propagating spectra are properly retained while upstream spectra are eliminated, with the tight clustering of upstream eigenvalues around zero demonstrating the efficacy of this approach.

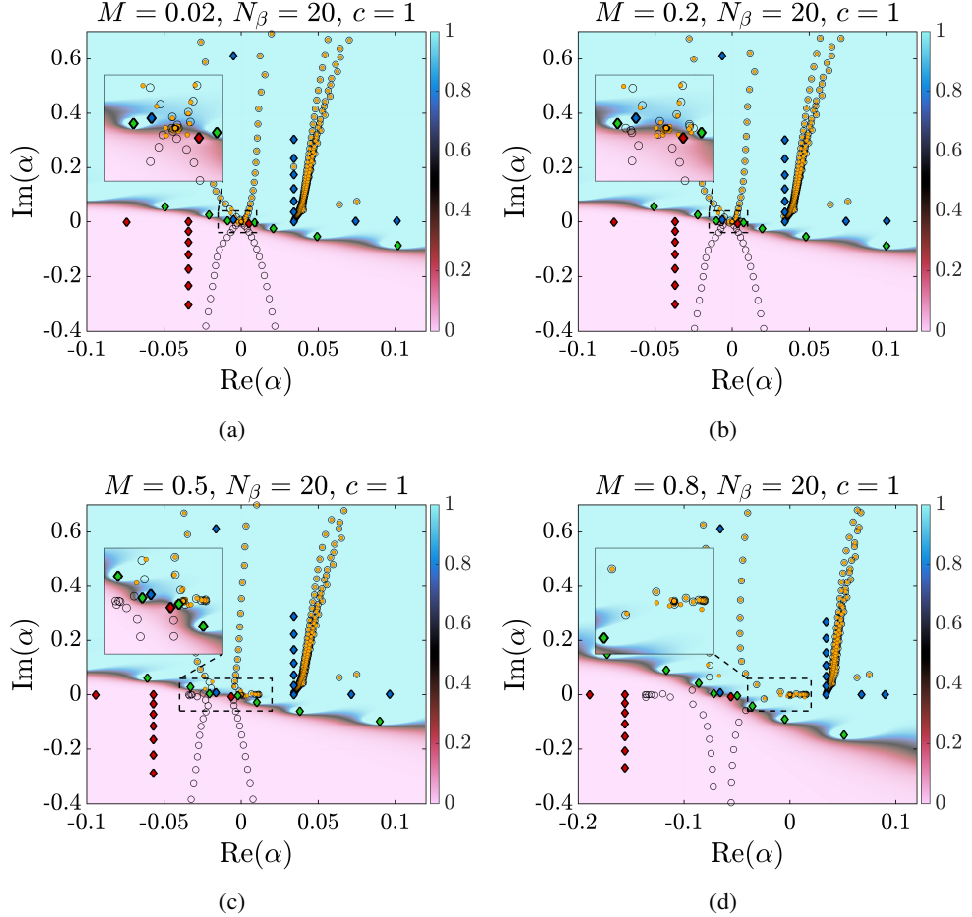


Fig. 3: Recursion selection algorithm for subsonic 2D-boundary layers at $R_\delta = 400$ with $b = 0$, $W = 0$ and $F = 86$ and variable Mach number. As M increases, the real parts of $\alpha_{4,5}$ become more pronounced.

Non-Uniform Distribution:

The need for non-uniform recursion parameter distributions arises from the distinction between continuous and discrete spectral representations. Whilst the continuous operator exhibits unbounded spectral branches, the discrete spectrum $\sigma(\mathbf{M})$ consists of a finite sampling of these branches, determined by the discretisation of the wall-normal direction.

This discretisation clusters collocation points near the wall, leading to a concentration of discrete eigenvalues near the real axis where $|\eta|$ is small. Conversely, the sparse distribution of points in the freestream corresponds to fewer eigenvalues with large imaginary parts, *i.e.*, where $|\eta|$ is large. Thus, the non-uniform spectral distribution necessitates a correspondingly non-uniform placement of recursion parameters: dense clustering near the real axis ensures adequate resolution of the concentrated eigenvalues, whilst wider spacing along the imaginary axis captures the increasingly sparse spectral content. The function y_{Malik} in Eq. (58) reflects this grid-induced spectral distribution, ensuring optimal placement of recursion parameters to filter the discrete approximation of the continuous spectrum.

These recursion parameters (not spectra) require recalculation at each streamwise location, as the spectra evolve spatially. Particular attention must be paid to tracking the discrete T-S wave as it migrates with increasing R_δ . Failure to maintain accurate tracking can lead to convergence difficulties or spurious migration to alternative eigenfunctions within the spectrum of \mathbf{M} .

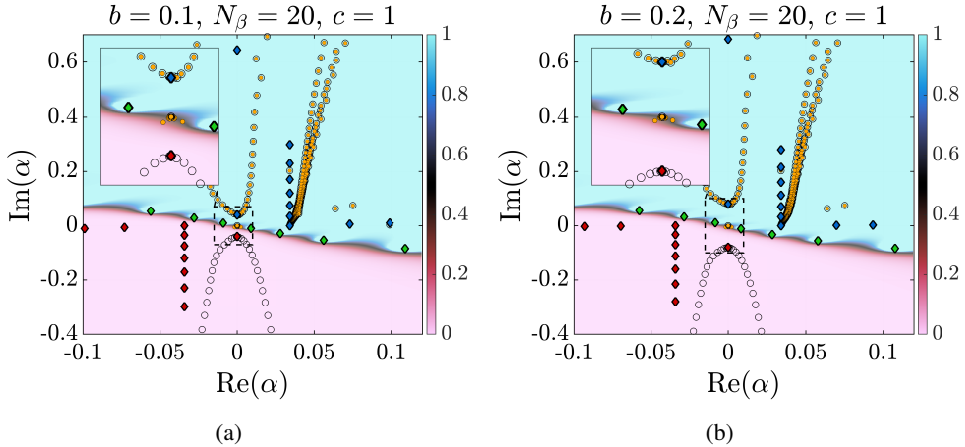


Fig. 4: Recursion selection algorithm for subsonic boundary layers with flow parameters $R_\delta = 400$, $M = 0.02$, $W = 0$ and $F = 86$ and $b = 0.1, 0.2$. As b increases, the acoustic branches separate moving up and down the imaginary axis. This makes the recursion parameter selection process much easier as the β^\pm parameters do not have to compete against each other.

Variable Mach and Spanwise Wavenumbers:

Figures 3 and 4 demonstrate that the recursion parameters defined in Eqs. (58) and (59) successfully parabolise cases with variable Mach number and spanwise wavenumber, respectively.

Disturbances with large spanwise wavenumber b exhibit considerably improved parabolisation characteristics compared to the two-dimensional case ($b = 0$). For large b , the upstream and downstream acoustic spectra become fully separated in the complex plane, eliminating the competition between β^+ and β^- recursion parameters and thereby reducing placement sensitivity significantly.

These parameters have been validated across a range of wall-normal discretisations (n_y ranging from 71 to 1201) and with the tuning parameter $c \in [0.2, 10]$ adjusted to achieve the requisite filtering strength for each configuration.

4.2.2 Forcing at the inlet with a Tollmien-Schlichting wave

Validation of M-OWNS proceeds through a systematic parametric analysis across compressibility (Mach number M) and 3D-obliqueness (b -parameter) of the disturbance. Each calculation is started at the inlet with a locally parallel flow (LST) approximation of a T-S wave eigenfunction.

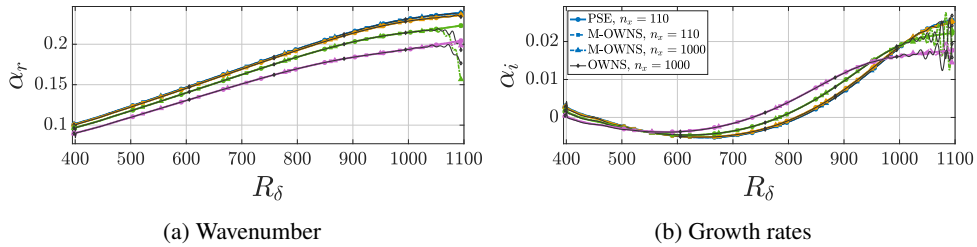


Fig. 5: (a) Wavenumber and (b) growth rates for a 2D-disturbance ($b = 0$) with $F = 86$ in a subsonic boundary layer with variable Mach number. (—) $M = 0.02$, (—) $M = 0.2$, (—) $M = 0.5$, (—) $M = 0.8$. All calculations include PSE with $n_x = 110$, M-OWNS with $n_x = 110$ and $n_x = 1000$, and OWNS at $n_x = 1000$. The agreement between the high-resolution and low resolution methods is excellent until the end of the computational march, where the high-resolution computations tend to be attracted (or migrate) towards a vorticity wave with wavenumber $d_1 = \alpha_{1,2,3}(0)$.

Figure 5 presents calculations for Mach numbers spanning $M = 0.02$ to $M = 0.8$, demonstrating that M-OWNS maintains agreement between low-resolution ($n_x = 110$) and high-resolution ($n_x = 1000$) computations, alongside corresponding PSE and OWNS results. This agreement persists throughout the evolution of wavenumber and growth rate until the terminal march stages, where high-resolution calculations exhibit a transition to vorticity wave behaviour characterised by $d_1 = \alpha_{1,2,3}(0)$. Similarly, Fig. 6 demonstrates equivalent consistency across spanwise wavenumber variations from $b = 0$ to $b = 0.3$ in incompressible boundary layers, confirming that M-OWNS accurately models three-dimensional disturbances.

The transition from T-S to vorticity waves observed in Fig. 6 arises from the complete eigenfunction representation inherent in the M-OWNS and OWNS operators. Whilst computations are initialised with a T-S eigenfunction from LST, this initial condition is inherently imperfect. The M operator intrinsically contains non-parallel terms and all eigenfunction

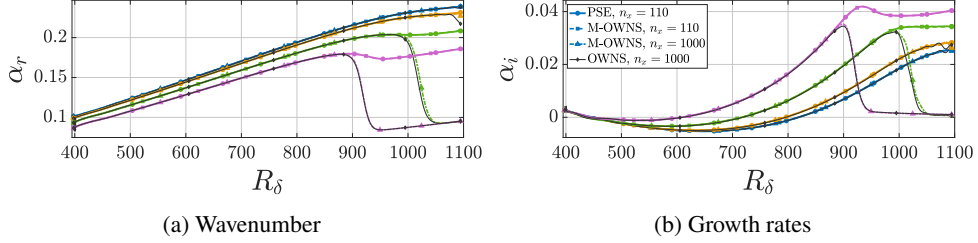


Fig. 6: (a) Wavenumber and (b) growth rates for a 3D-disturbance with $F = 86$ and variable spanwise wavenumber in an incompressible boundary layer ($M = 0.02$). (—) $b = 0$, (—) $b = 0.1$, (—) $b = 0.2$, (—) $b = 0.3$. All calculations include PSE with $n_x = 110$, M-OWNS with $n_x = 110$ and $n_x = 1000$, and OWNS at $n_x = 1000$. Note the excellent agreement between the high-resolution and low resolution methods. At the end of the computational march the high-resolution results then migrate to a vorticity wave with wavenumber $d_1 = \alpha_{1,2,3}(0)$.

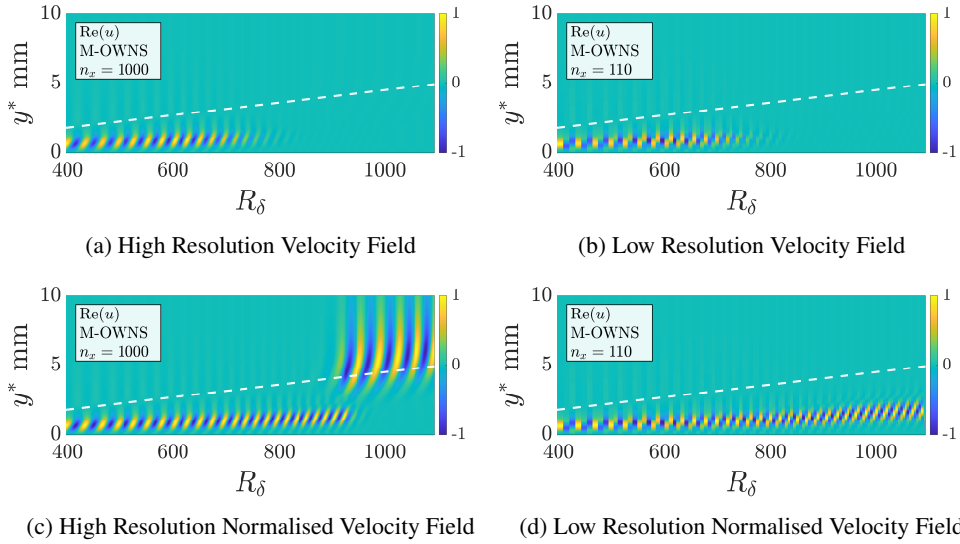


Fig. 7: Streamwise velocity disturbance profiles for a disturbance with $F = 86$ in an incompressible 2D boundary layer ($M = 0.02$) with spanwise wavenumber ($b = 0.3$). The velocity has been normalised (in plots c and d) by the maximum locally to show the shape of the wave.

components, including the vorticity wave contribution. As computations proceed downstream and the T-S wave undergoes exponential decay, the more slowly decaying vorticity wave, initially orders of magnitude weaker, eventually dominates the solution. This transition manifests dramatically in the weighted average wavenumber calculation, Eq. (26), where α_r rapidly shifts from T-S to vorticity wave values at $R_\delta \approx 900$. An alternative explanation is this is a

phenomena associated with OWNS-type calculations; ultimately more study is needed on this behaviour.

Figure 7 reveals pronounced resolution dependence in capturing this phenomenon. Coarse meshes ($n_x = 110$) fail to resolve the transition as the deteriorating T-S wave structure becomes under resolved, whilst fine meshes ($n_x = 1000$) accurately track the emergence of the vorticity wave. The PSE exhibits behaviour analogous to coarse-mesh calculations, whereas high-resolution OWNS and M-OWNS successfully capture the transition to vorticity-dominated flow structures, as shown in Fig. 7c.

M-OWNS addresses a critical computational deficiency in the intermediate discretisation regime where $n_x \sim 200$. Figure 8 demonstrates that both PSE and OWNS encounter significant numerical difficulties in this range. The PSE cannot operate beyond its step-size constraint, whilst standard OWNS exhibits oscillations leading to computational breakdown; OWNS only converges to accurate results with substantially finer x -resolution. In contrast, M-OWNS maintains numerical stability throughout the domain for all resolutions tested.

OWNS Step-Size Limitation

While normalised quantities such as wavenumber require relatively modest resolution, accurate prediction of disturbance amplitude and energy demands significantly finer x -discretisation with standard OWNS. Fig. 9, computed for an incompressible two-dimensional boundary layer with $F = 86$, demonstrates that OWNS requires $n_x > 8000$ for converged disturbance amplitude and energy estimates. The results reveal systematic under-prediction of kinetic energy and velocity magnitudes at moderate resolutions, necessitating approximately 200 points per wavelength for accurate amplitude predictions.

Similar resolution requirements emerge in compressible flows. Fig. 10 compares PSE, OWNS, and M-OWNS energy predictions for a Mach 0.8 two-dimensional boundary layer, using first-order (BFD1) and second-order (BFD2) x -discretisations with convergence criterion $\varepsilon = 10^{-9}$. The OWNS energy predictions increase gradually with streamwise resolution, achieving agreement with M-OWNS only at extreme discretisations ($n_x > 4000$). The vertical dashed line indicates the PSE resolution limit of 2π points per wavelength ($n_x \approx 145$), beyond which PSE fails to converge. As expected, OWNS with first-order differencing exhibits the poorest performance; even with $n_x > 10000$, the wave-varying components remain severely under-resolved.

In contrast, M-OWNS demonstrates convergent behaviour across the entire resolution range, maintaining consistent energy predictions with as few as 10^2 streamwise points. These results reveal the computational efficiency of M-OWNS, indicating potential computational savings of two orders of magnitude relative to standard OWNS. Thus, M-OWNS successfully combines the computational efficiency of modal methods with the robustness of OWNS, remaining stable at resolutions where PSE encounters step-size constraints and standard OWNS exhibits either numerical instability or insufficient convergence.

4.3 Swept Cylinder Flow

To demonstrate M-OWNS capabilities in three-dimensional flows, we consider the incompressible boundary layer over a swept cylinder with radius 0.5 m and sweep angle 65° , corresponding to a crossflow Reynolds number $R = 500$ as studied by Malik et al. [37]. This

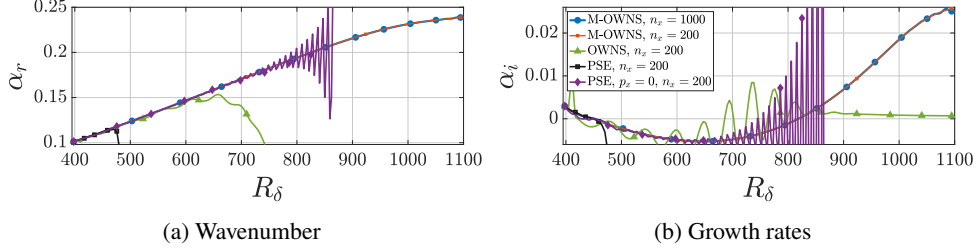


Fig. 8: (a) Wavenumber and (b) growth rates for a disturbance with $F = 86$ in an incompressible boundary layer ($M = 0.02$) with zero spanwise wavenumber ($b = 0$). Only M-OWNS gives consistent and converged results with $n_x = 200, 1000$; both OWNS and PSE ($p_x = 0$) fail on using $n_x = 200$ points, while PSE with p_x retained has the worst behaviour.

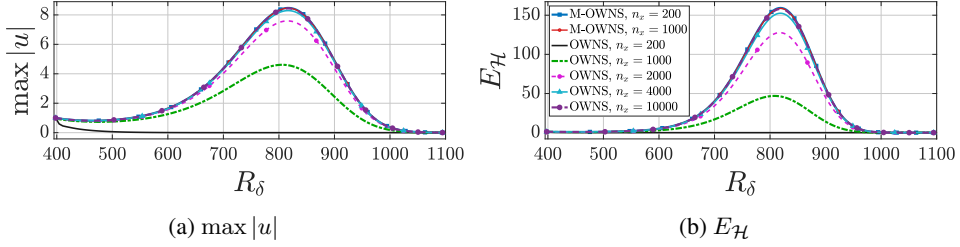


Fig. 9: (a) Maximum streamwise velocity magnitude and (b) disturbance energy for a disturbance with $F = 86$ in an incompressible 2D boundary layer ($M = 0.02$) with zero spanwise wavenumber ($b = 0$). Here again, observe only M-OWNS gives consistent results on varying n_x .

configuration introduces additional complexities in recursion parameter selection due to the three-dimensional boundary layer structure.

The flow configuration exhibits streamwise acceleration with $U \sim C^*x$ (where C^* is constant), whilst the spanwise velocity W varies with x as it is locally normalised by U . The dimensional curvature metric term $\bar{\kappa} = 2/m$ is included as defined in Eq. (A1). For our fully compressible formulation, we set the freestream temperature $T_\infty = 300$ K and $M = 0.0001$. All calculations employ $n_y = 301$ wall-normal points over the streamwise domain $132 \leq R_\delta \leq 1460$.

The OWNS computations are initialised with LST eigenfunctions at $R_\delta = 132$, using $N_\beta = 20$ recursion parameters for the streamwise integration. We examine two crossflow disturbances at fixed spanwise wavenumber $\beta = 0.4$: a stationary mode ($\omega = 0$) and a travelling mode with frequency $F = \omega/R \times 10^6 = 75$.

The three-dimensional flow introduces a key computational challenge: the vorticity/entropy branches evolve dynamically with x as the M-OWNS computation progresses. Figs. 11a and 11b illustrate the spectra at distinct streamwise locations, revealing that the

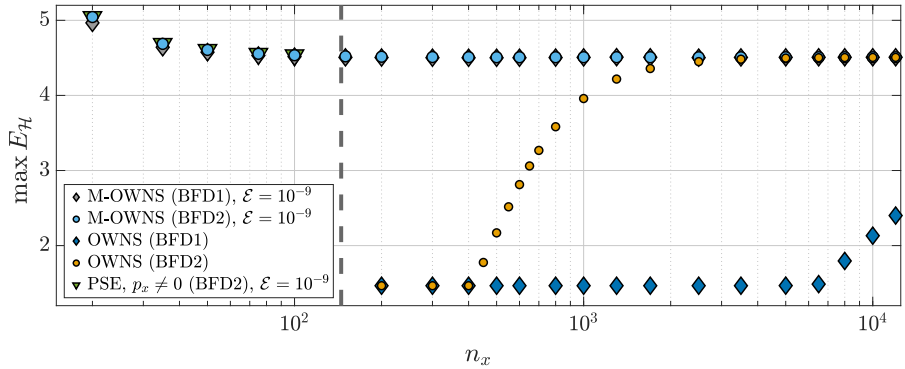


Fig. 10: Maximum density-scaled kinetic energy (E_H) versus streamwise resolution (n_x) for a $M = 0.8$ flat-plate boundary layer, with $b = 0.1$ and frequency $F = 150$.

vorticity/entropy branches $\alpha_{1,2,3}$ migrate towards the acoustic spectra as W/U decreases downstream. This migration creates parameter competition, as the β^+ recursion parameters placed on vorticity/entropy branches increasingly interfere with the β^- parameters targeting upstream-propagating acoustic modes.

The recursion parameters defined by Eqs. (58) and (59) accommodate this three-dimensional behaviour through two mechanisms. First, the symmetric placement of β^\pm parameters about d_2 maintains balanced filtering strength despite the spectral migration. Second, the imaginary extent of vorticity/entropy parameter placement naturally contracts downstream through the $|\alpha_0|$ scaling factor in Eq. (58). At each streamwise location, we recalculate the continuous spectra positions and adjust the recursion parameters accordingly, bounding their placement to track the spectral evolution. This adaptive approach ensures both numerical stability and accurate capture of the evolving crossflow disturbances throughout the spatial march.

Figure 12 demonstrates excellent agreement between PSE, M-OWNS, and OWNS-R in modelling both stationary and travelling crossflow disturbances. However, convergence analysis in Fig. 13 reveals substantial differences in computational efficiency. Whilst OWNS-R requires $n_x > 8000$ points for converged energy predictions, M-OWNS achieves comparable accuracy with only $n_x \geq 150$ points, a reduction of two orders of magnitude in computational cost. These results confirm that M-OWNS maintains its efficiency advantages in three-dimensional flows with evolving spectra.

4.4 Supersonic Boundary Layer

This section demonstrates M-OWNS capabilities for supersonic flows where multiple discrete eigenvalues coexist in the spectrum of \mathbf{M} . We examine a Mach 4.5 boundary layer, following Mack [24], to investigate multimodal interactions and non-modal phenomena. Three distinct forcing scenarios are analysed: (i) inlet forcing with Mode S to study mode synchronisation, (ii) fast acoustic wave forcing to examine receptivity mechanisms, and (iii) wall blowing-suction to

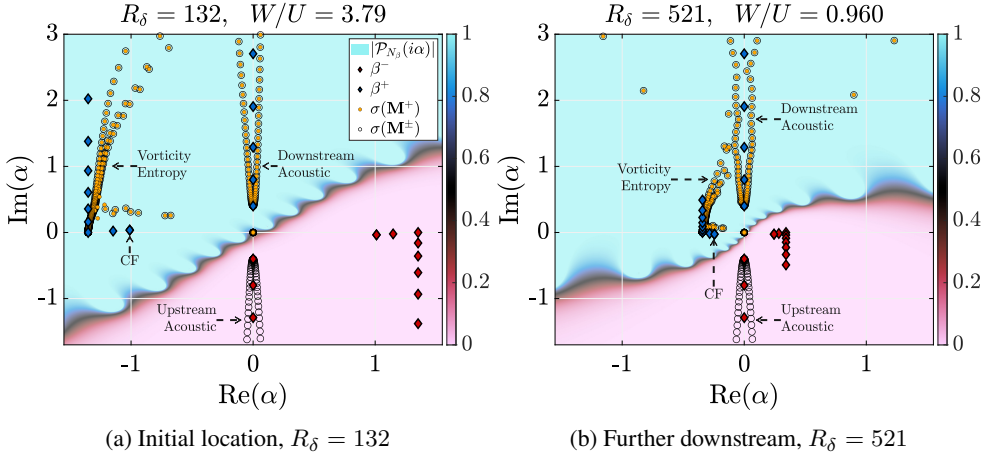


Fig. 11: Evolution of eigenvalue spectra for the swept cylinder ($R = 500$). Panels show (a) initial station $R_\delta = 132$ and (b) downstream station $R_\delta = 521$. Note the migration of the discrete CF wave and vorticity/entropy branches towards the acoustic branch as R_δ increases.

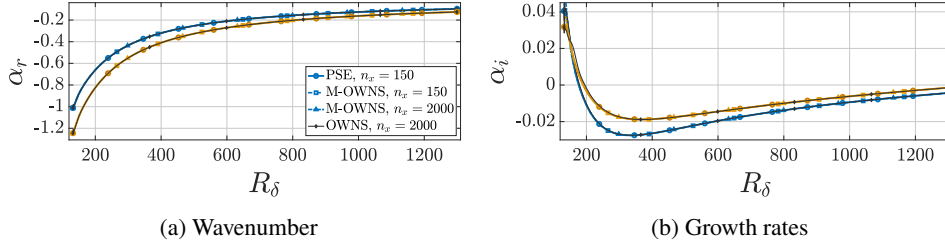


Fig. 12: (a) Wavenumber and (b) growth rates for CF disturbances ($\beta = 0.4$) in the swept cylinder analysis. Results shown for (—) travelling ($F = 75$) and (—) stationary ($F = 0$) crossflows. Computations performed using PSE ($n_x = 150$), M-OWNS ($n_x = 150, 2000$), and OWNS ($n_x = 2000$).

explore multimodal excitation. Our results demonstrate that M-OWNS captures these complex phenomena with two orders of magnitude fewer streamwise points than standard OWNS.

4.4.1 Mode Classification and Synchronisation

Supersonic boundary layers support two primary instability modes with distinct physical origins. Following the classification of Mack [24], the first mode represents the compressible analogue of T-S waves, whilst the second mode, unique to compressible flows, consists of acoustic waves trapped between the wall and the relative sonic line.

Fedorov [38] provides an alternative framework, identifying the discrete modes as slow (S) and fast (F) modes that synchronise with their respective acoustic spectra near the leading

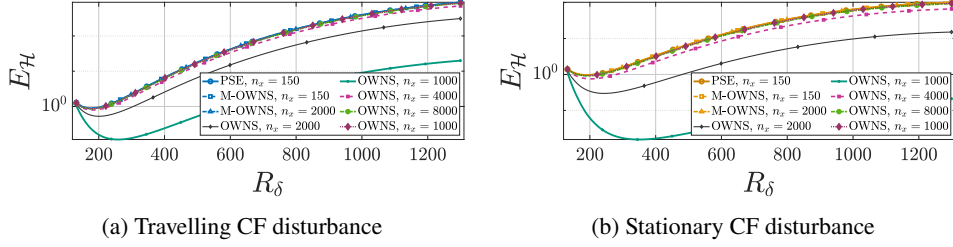


Fig. 13: Energy evolution of CF disturbances ($\beta = 0.4$) in the swept cylinder analysis. Panels show (a) travelling ($F = 75$) and (b) stationary ($F = 0$) disturbance analysis. Comparison includes PSE ($n_x = 150$), M-OWNS ($n_x = 150, 2000$), and OWNS at various streamwise resolutions.

edge. We denote the associated continuous spectral branches as slow acoustic (SA) and fast acoustic (FA). Far downstream, the S and F mode wavenumbers coalesce, the modes synchronise, and efficient inter-modal energy transfer occurs [39]. This synchronisation constitutes a fundamental non-modal phenomenon.

The S-F synchronisation point marks a critical transition in stability characteristics. Prior to synchronisation, mode S exhibits first-mode growth characteristics whilst mode F remains stable or weakly damped. Beyond the synchronisation point, the coupled system radiates acoustic energy and transitions to second-mode behaviour, becoming the dominant instability mechanism [40]. This modal interaction and subsequent acoustic radiation present significant computational challenges that we address through the M-OWNS formulation.

4.4.2 Flow Configuration and Test Cases

We adopt the flow conditions from Ma and Zhong [41]: $M = 4.5$, $R_\infty = 7.2 \times 10^6 \text{ m}^{-1}$, $T_\infty = 65.15 \text{ K}$, $p_\infty = 728.44 \text{ Pa}$, and Prandtl number $\sigma = 0.72$. The disturbance frequency $F = 220$ and spanwise wavenumber $b =$ matches that investigated by Zhu and Towne [14] in developing the OWNS-R method. We impose the adiabatic temperature condition $T_y = 0$ at the wall. Three forcing scenarios probe different aspects of the multimodal dynamics:

1. **Mode S forcing:** Direct excitation of the slow mode at the inlet naturally exhibits non-modal behaviour through S-F synchronisation, allowing assessment of M-OWNS performance in capturing modal energy transfer.
2. **Fast acoustic wave forcing:** A planar inviscid freestream acoustic wave excites multiple boundary layer eigenfunctions simultaneously, producing non-modal characteristics through modal superposition.
3. **Wall forcing:** Blowing and suction at the wall generates non-modal response via simultaneous excitation of discrete and continuous spectral components.

4.4.3 Recursion Parameter Selection

The supersonic flow spectrum differs fundamentally from subsonic cases, requiring a modified recursion parameter strategy. Fig. 14 illustrates the spectral topology, whilst Fig. 15 presents the detailed structure at $R_\delta = 400$ with $n_y = 121$.

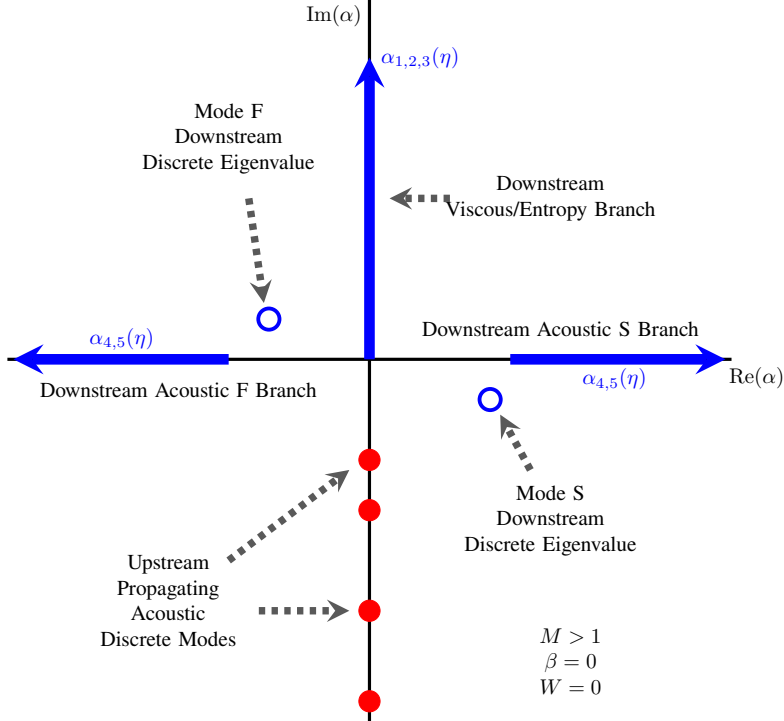


Fig. 14: Spectral structure of the streamwise spatial marching operator \mathbf{M} , for a supersonic boundary layer under the parallel flow assumption. The supersonic spectrum contains no upstream continuous branches but possesses upstream-propagating discrete acoustic modes alongside downstream discrete modes (Mode S and Mode F). Arrows denote the direction of increasing η^2 along each branch.

Unlike subsonic flows, all continuous acoustic branches in supersonic boundary layers propagate downstream. Upstream propagation occurs only through discrete acoustic modes, trapped between the wall and sonic line, that decay exponentially [36]. These upstream modes populate the negative imaginary half-plane with increasing density as $\text{Im}(\alpha)$ decreases.

To accommodate this spectral structure, we employ distinct strategies for β^+ and β^- parameters:

Downstream Parameters (β^+):

We position these non-uniformly along the vorticity/entropy branches to capture all downstream-propagating modes:

$$\beta_j^+ = d_1 + iy_{\text{Malik}} \left(\frac{j-1}{N_\beta - 1}, 0.2, 5 \right), \quad (61)$$

where y_{Malik} provides the non-uniform distribution defined in Eq. (50). This placement ensures retention of discrete S and F modes alongside the continuous spectra.

Upstream Parameters (β^-):

These target the upstream-propagating discrete modes through enhanced clustering near the real axis:

$$\beta_j^- = -0.15 - 0.01i - (10(-1)^j + 50i) y_{\text{Malik}} \left(\frac{j-1}{N_\beta - 1}, 0.01, 1 \right). \quad (62)$$

The alternating term $(-1)^j$ provides lateral spreading whilst maintaining dense coverage near $\text{Im}(\alpha) = 0$.

This configuration, illustrated in Fig. 15, employs $N_\beta = 30$ recursion parameters with filtering strength $c = 0.5$. These values, optimised for the present Mach 4.5 configuration, achieve complete downstream spectrum retention whilst eliminating upstream propagation.

4.4.4 Mode S Forcing Results

We examine Mode S forcing at the inlet, extending the analysis of Zhu and Towne [14]. The computational domain spans $R_\delta = 400$ to 1410 with $n_y = 600$ wall-normal points, with the second-order BFD2 discretisation in x .

Figure 16 reveals a striking disparity in convergence behaviour between OWNS-R and M-OWNS. The standard OWNS exhibits severe resolution dependence: wall pressure predictions vary significantly with streamwise discretisation, requiring $n_x \sim 8000$ points for convergence (see Fig. 16a). In contrast, M-OWNS achieves converged wall pressure distributions with all discretisations tested, demonstrating robust performance even at modest resolutions, as is apparent in Fig. 16b.

The true advantage of M-OWNS emerges in resolving the acoustic radiation field generated by S-F synchronisation. Fig. 17 compares pressure fields at two resolutions: $n_x = 12000$ (reference) and $n_x = 2000$. At the finer resolution, both methods successfully capture the near-wall second mode and its acoustic radiation into the freestream. However, at $n_x = 2000$, OWNS fails to resolve the radiation pattern, producing an inaccurate pressure field while M-OWNS maintains both near-wall accuracy and radiation field structure.

This sixfold reduction in resolution requirement stems from M-OWNS's weighted-average wavenumber formulation (Eq. (26)); rather than tracking mode S alone, α represents the superposition of all active modes at each streamwise location. The modal shape function provides the flexibility to capture evolving dynamics automatically, whether dominated by single modes or exhibiting multimodal characteristics.

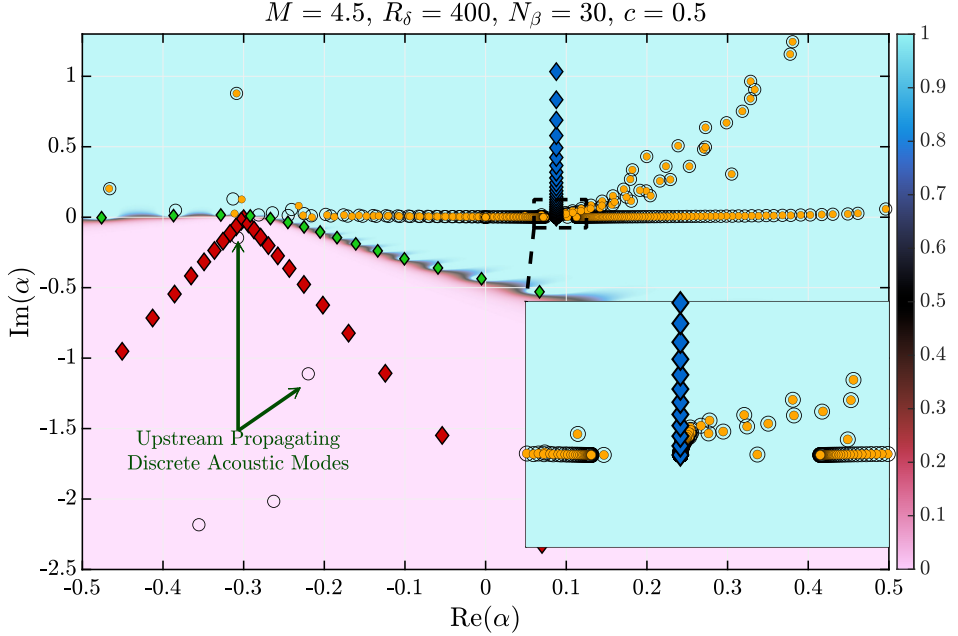


Fig. 15: Numerical spectrum of the two-way system $\sigma(\mathbf{M}^\pm) = \sigma(\mathbf{M})$ and the parabolised downstream system $\sigma(\mathbf{M}^+) = \sigma(\mathbf{P}_{N_\beta}\mathbf{M})$ for a supersonic flat-plate boundary layer ($M = 4.5$, $R_\delta = 400$, $N_\beta = 30$, $c = 0.5$). Downstream eigenvalues are preserved whilst upstream eigenvalues are eliminated.

These results address a fundamental question raised by Zhu and Towne [14]: can modal methods capture acoustic radiation from mode synchronisation? Their PSE calculations, limited to $n_x = 323$ points, failed to resolve the radiation field. Our M-OWNS results demonstrate that the modal ansatz itself does not preclude capturing non-modal phenomena, rather PSE's step-size limitation prevents the adequate resolution. M-OWNS operates successfully with $n_x \geq 650$ points (exceeding PSE stability limits) and yet requires far fewer points than standard OWNS, effectively bridging the gap between modal efficiency and non-modal capability.

4.4.5 Fast Planar Acoustic Wave Forcing

We next examine receptivity to fast planar acoustic waves, following Ma and Zhong [41, 43]. The computational domain extends from $R_\delta = 275$ to 1272 with $n_y = 800$ wall-normal points. The incident acoustic wave takes the form $\phi(0) = |\phi| \exp(ikx - i\omega t)$, where the wavenumber $k = \omega M / (1 + M)$, with amplitude components:

$$|u| = 1, \quad |p| = |u|/M, \quad |T| = (\gamma - 1)M|u|, \quad |v| = 0, \quad |w| = 0. \quad (63)$$

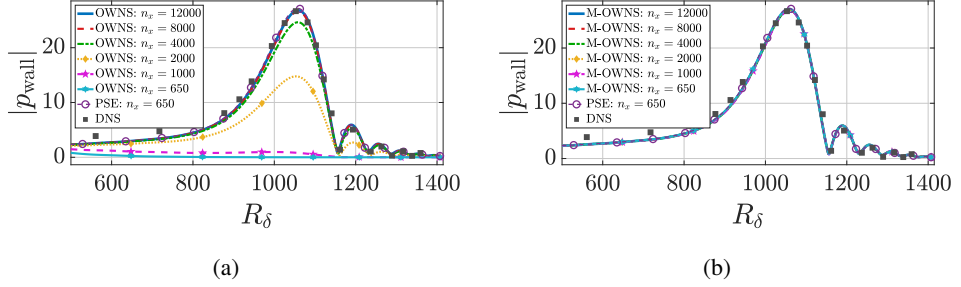


Fig. 16: Wall pressure amplitude ($|p_{\text{wall}}|$) for a Mach 4.5 boundary layer at $F = 2.2 \times 10^{-4}$, comparing (a) OWNS-R and (b) M-OWNS implementations across varying streamwise discretisations. DNS reference solution from Ma and Zhong [42]. The OWNS-R solution exhibits strong dependence on streamwise discretisation, whilst M-OWNS achieves convergence for all discretisations.

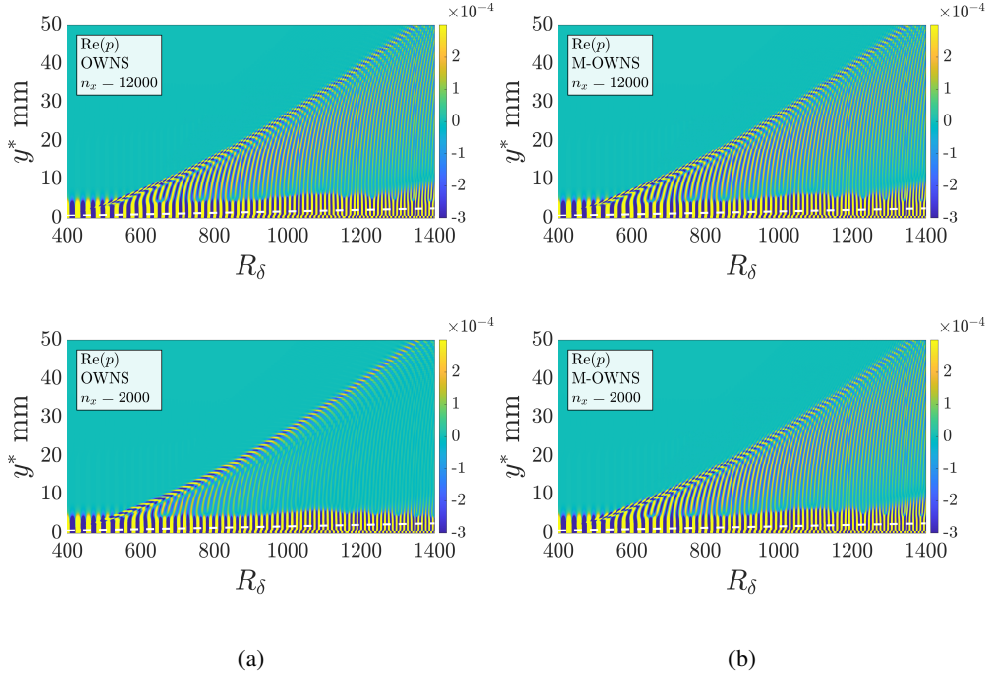


Fig. 17: Real pressure field $|p|$ for S mode forcing in a Mach 4.5 boundary layer, comparing OWNS (left column) and M-OWNS (right column) with $n_x = 12000$ (top row) and $n_x = 2000$ (bottom row) streamwise points. M-OWNS captures the acoustic radiation field at a coarser resolution, whilst OWNS requires substantially finer discretisation for accurate representation.

This forcing configuration provides a stringent test of M-OWNS capabilities for non-modal phenomena. The incident fast acoustic wave impinges upon the wall, exciting multiple disturbance modes within the spectrum of M. The subsequent evolution involves complex modal interactions and energy exchange that challenges traditional stability analysis methods.

Figure 18 reveals the complete synchronisation sequence captured by M-OWNS. Initially, the fast acoustic wave synchronises with Mode F near the inlet, evident in the wavenumber evolution (Fig. 18a) tracking the F-mode branch. As the disturbance propagates downstream, energy cascades through modal interactions, culminating in S-F synchronisation near $R_\delta \approx 1000$. This critical transition manifests as a pronounced spike in growth rate (Fig. 18b), marking the onset of second-mode behaviour.

Significantly, the wavenumber does not simply switch from F to S mode characteristics. Instead, it maintains intermediate values representing the weighted superposition of multiple active modes – a fundamentally non-modal response that M-OWNS captures through its wavenumber evaluation.

The resolution requirements reveal M-OWNS's computational advantage most clearly. At $n_x = 1000$ points, standard OWNS fails completely: the solution exhibits spurious oscillations and misses the synchronisation event entirely. Conversely, M-OWNS at this coarse resolution accurately reproduces the modal evolution obtained by OWNS at $n_x = 5000$, *i.e.* a five-fold reduction in computational requirements.

This efficiency gain extends to the complete flow field. Fig. 19 compares pressure fields at both resolutions. With $n_x = 5000$, both methods successfully resolve the characteristic acoustic radiation patterns and boundary layer modulation. However, at $n_x = 1000$, OWNS produces unphysical results whilst M-OWNS maintains accuracy throughout the domain. The wall-normal pressure distributions (Fig. 20) confirm that M-OWNS performs equally well in the boundary layer and in the far-field acoustic radiation zone.

These results demonstrate that the modal ansatz, when properly implemented with wavenumber extraction, provides computational benefits even for inherently non-modal phenomena. The efficiency stems not from restricting the solution to single modes, but from the representation of multimodal superpositions through the evolving shape function. This finding challenges the conventional view that modal methods cannot capture non-modal physics, suggesting instead that implementation limitations, such as PSE's step-size constraints, have historically prevented their application to complex flows.

4.4.6 Wall Forcing via Suction and Blowing

The final test case examines disturbance generation through wall suction and blowing, following the detailed investigation of Ma and Zhong [41, 43]. We adopt their wall forcing function:

$$v_{\text{wall}}(x') = \begin{cases} a_0 \sin(2\pi(\bar{x} - \bar{x}_0)/\bar{x}_l), & \text{if } |\bar{x} - \bar{x}_0| \leq \bar{x}_l/2 \\ 0, & \text{otherwise,} \end{cases} \quad (64)$$

where $\bar{x}_0 = 0.0125$ m (corresponding to $R_\delta = 300$), $\bar{x}_l = 0.0029127$ m, and a_0 is an arbitrary amplitude coefficient. The forcing extends over $282 \leq R_\delta \leq 317$, with an adiabatic wall condition $T_y = 0$ imposed throughout.

This forcing configuration presents unique challenges for modal methods. The imposed spatial scales are significantly smaller than PSE's minimum stable step-size, precluding its

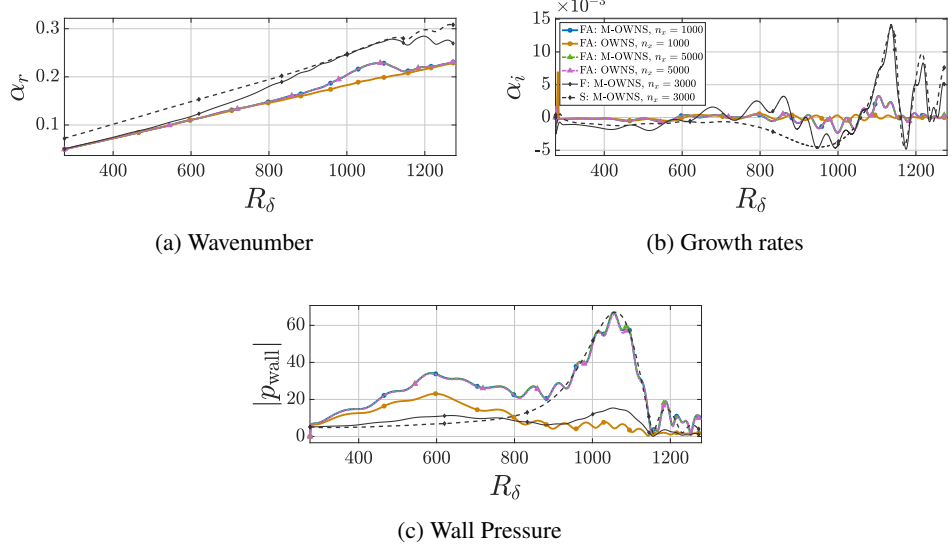


Fig. 18: Evolution of (a) wavenumber α_r , (b) growth rate α_i , and (c) wall pressure $|p_{\text{wall}}|$ for fast acoustic wave forcing. M-OWNS at $n_x = 1000$ captures the modal synchronisation sequence, matching OWNS at $n_x = 6000$, whilst a lower resolution OWNS computation fails to resolve the physics correctly. The direct S and F, M-OWNS calculations are shown for reference.

application. For OWNS calculations, the forcing term must be parabolised using the projection operator at each streamwise location where forcing is active to maintain numerical stability.

Linear stability analysis indicates that Mack's second mode becomes unstable at $R_\delta \approx 804$ and returns to stability at $R_\delta \approx 1080$. The wall forcing generates significant transient non-modal fields that evolve through several stages: initial transient response, formation of weakly stable Mack waves, continued non-modal interactions, and finally establishment of the second mode in the synchronisation region.

Figure 21 demonstrates that M-OWNS successfully captures this complex initialisation scenario. The normalised wall pressure magnitude shows excellent agreement with high-resolution OWNS and LHNS computations, whilst standard OWNS with $n_x = 1000$ severely under-predicts the amplitude. Figures 22(a–f) present detailed comparisons between M-OWNS, OWNS, and LHNS for the evolving disturbance temperature and pressure fields. The temperature disturbances exhibit maxima near the boundary layer edge with secondary peaks at the wall, consistent with Ma and Zhong [41], see also Fig. 23. The much weaker pressure disturbances ($\sim 1/60$ weaker in magnitude) peaks at the wall and decays with wall-normal distance.

All methods capture the oblique compression wave generated by the wall forcing, propagating according to Mach wave theory with negligible upstream influence behind the wavefront. The M-OWNS and LHNS temperature fields, Fig. 22(d,f), are nearly identical. While the LHNS computed pressure field shown in Fig. 22e indicates weak pressure reflections of outgoing signals interacting with the initial compression wave, bouncing back towards, and reflecting from the boundary layer edge at about $R_\delta \sim 600$: a feature not picked up by

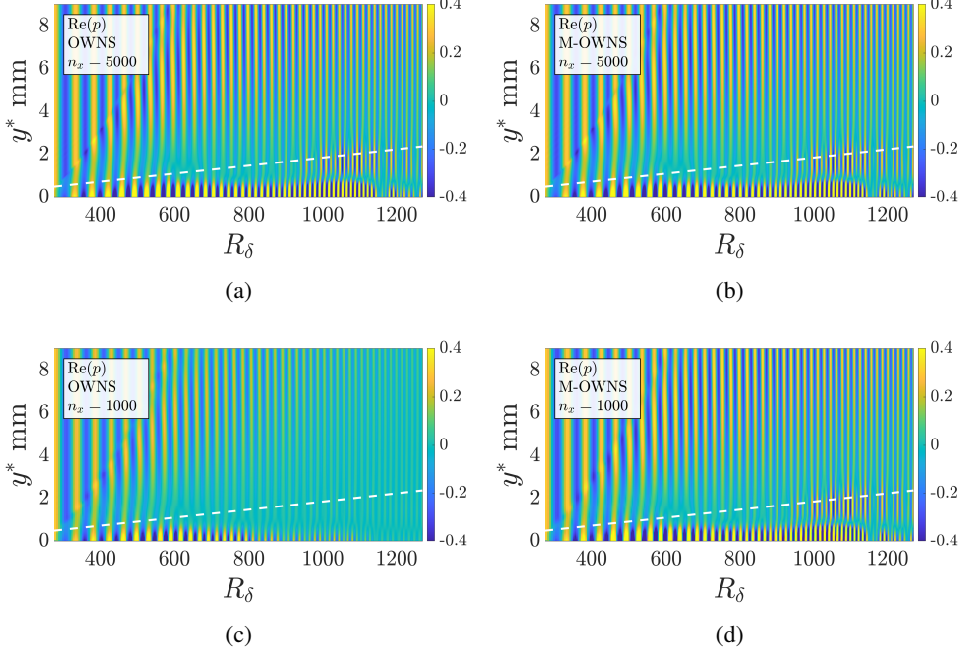


Fig. 19: Pressure field $\text{Re}(p)$ for fast acoustic wave forcing comparing (a,b) OWNS and M-OWNS at $n_x = 5000$, and (c,d) at $n_x = 1000$, with the white dashed line the boundary layer edge. M-OWNS maintains physical accuracy at coarse resolution whilst OWNS degrades catastrophically.

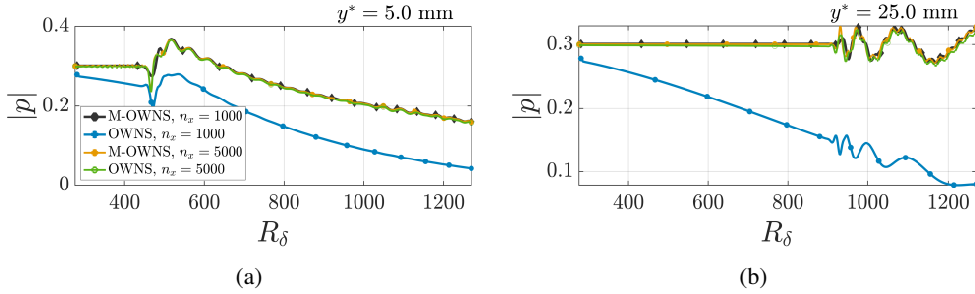


Fig. 20: Pressure magnitude $|p|$ at $y^* = 5.0$ mm and $y^* = 25.0$ mm. M-OWNS captures the modal content throughout the computational domain, even at modest resolution, demonstrating robust performance for multimodal disturbances.

M-OWNS in Fig. 22c. Conversely, the pressure field of M-OWNS suggests extremely weak pressure fluctuations behind the wavefront, which the LHNS does not feature.

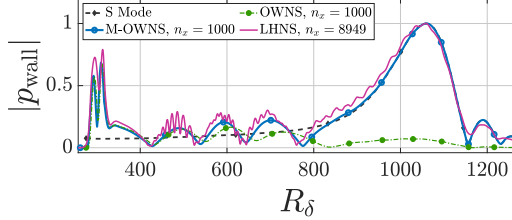


Fig. 21: Normalised wall pressure magnitude $|p|$ for the $M = 4.5$ boundary layer. The dashed black (S) M-OWNS curve is computed with M-OWNS forced with a slow mode eigenfunction at inflow. The surface suction/blowing given by Eq. (64) has a sine-wave variation over the Reynolds number range : $282 \leq R_\delta \leq 317$.

Despite apparent disagreement between low-resolution OWNS and other methods in the field plots, the normalised disturbance profiles (Fig. 23) extracted at $R_\delta \sim 1050$ show remarkable agreement across all methods. This apparent paradox reveals fundamental insights into the numerical behaviour. OWNS at low resolution successfully captures the wall-normal shape function but cannot resolve the streamwise wave-like variations. The normalisation process removes the exponential growth and phase information, extracting only the eigenfunction structure at each location. This explains why normalised profiles agree whilst the full disturbance fields differ dramatically: low-resolution OWNS captures the local modal shape but not the spatial evolution of amplitude and phase. This observation validates the M-OWNS approach. By explicitly separating the wave-like component through the modal ansatz, M-OWNS efficiently captures both the shape function and its spatial evolution, achieving at modest resolution what standard OWNS requires considerably more points to resolve the wave behaviour.

Minor discrepancies in results, between LHNS and M-OWNS, near the wall likely arise from a number of sources: differences in implementing the adiabatic temperature condition, or effects of the projection operator removing elliptic pressure/temperature components in regions where upstream-propagating discrete modes are significant. It should be noted that signals can propagate upstream in the subsonic sub-layer of the boundary layer, which M-OWNS restricts and the LHNS captures in its entirety. The upstream signals no doubt contribute to the observed differences, between LHNS and M-OWNS, particularly around the forcing region as the actuation is applied at the surface.

We have focussed on comparing temperature and pressure fluctuations, with pressure the weakest component of the disturbance fields. Otherwise excellent agreement is observed, in the larger in magnitude velocity fields too (not shown here). Overall, the observed minor differences may be due to model dependency and possibly under-resolution with the LHNS (particularly so), which was run with the maximum computer memory available to us. But generally differences remain small and do not affect the overall excellent agreement between methods or the conclusions to be drawn.

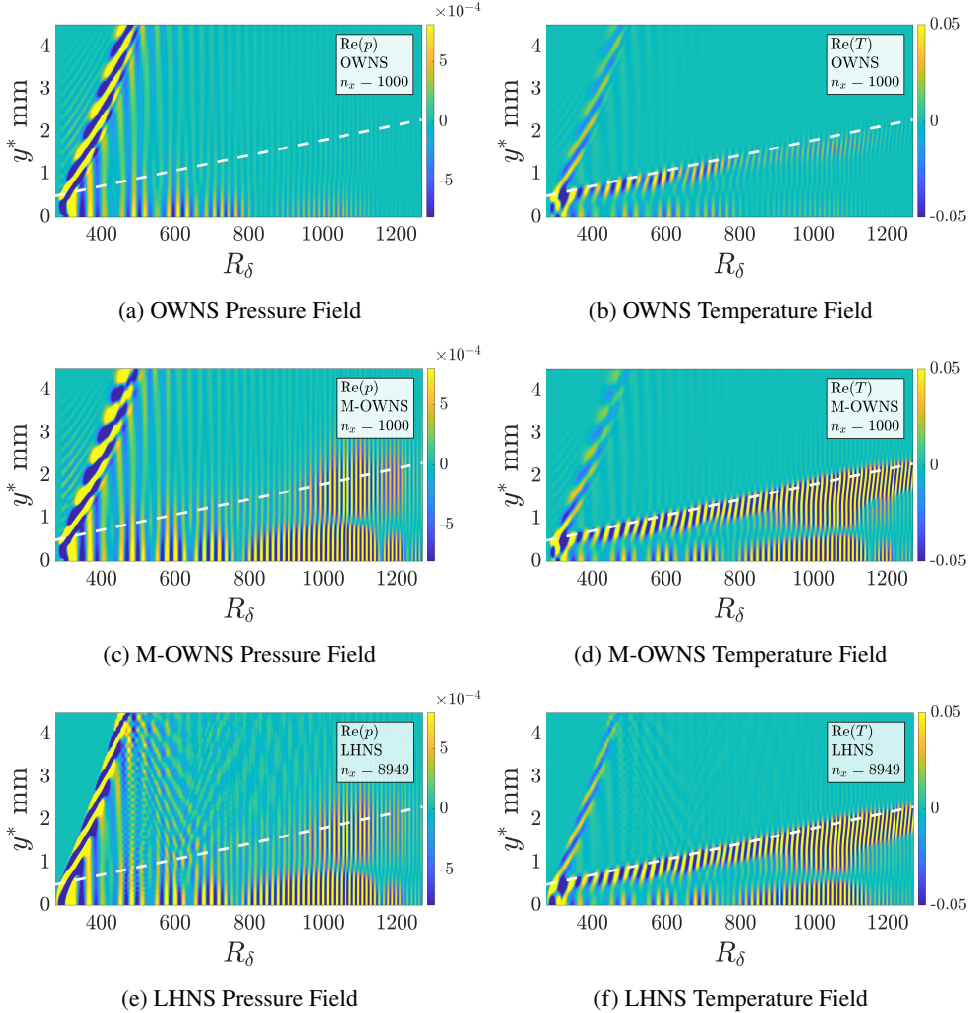


Fig. 22: The complete disturbance pressure p (left) and temperature T (right) fields computed with OWNS, M-OWNS and LHNS for the $M = 4.5$ boundary layer forced by surface suction-blowing in the region $282 \leq R_\delta \leq 317$. The white dashed line denotes the boundary layer edge.

4.5 Computational Time

The computational efficiency of stability analysis methods depends critically on spatial resolution requirements and iterative convergence behaviour. To quantify the efficiency gains achieved through our modal formulation, we next compare the computational costs of PSE, OWNS-R, and M-OWNS.

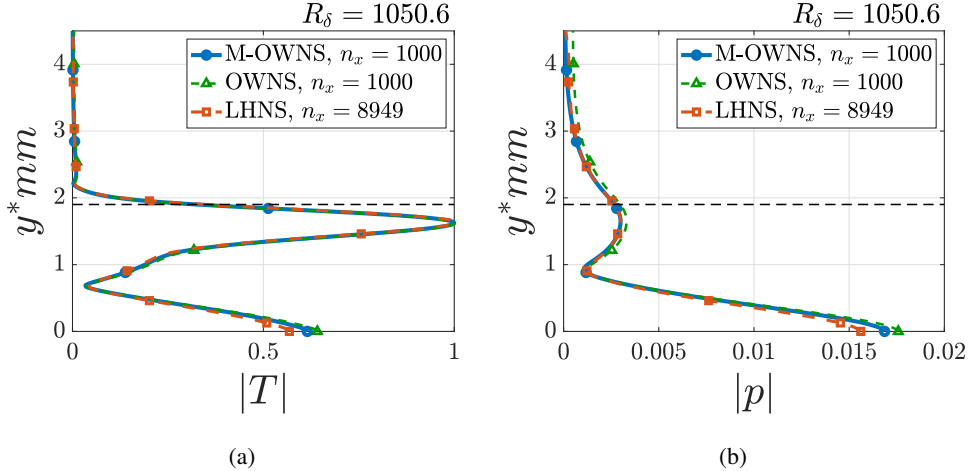


Fig. 23: M-OWNS and OWNS calculations at $n_x = 1000$, and LHNS at $n_x = 8949$, compared at $R_\delta = 1050.6$ for $M = 4.5$ case. The temperature disturbance maximum is normalised to unity. Although the OWNS results have the correct shape, the true max. temperature value was 0.0241, whereas the true max. value of the M-OWNS was 0.4981 – a factor of 20. The slight differences at $y^* = 0$ are due to the projection operator acting upon the M-OWNS disturbance; dashed line denotes the boundary layer edge.

PSE achieves exceptional computational efficiency through two mechanisms. First, the modal ansatz enables accurate disturbance modelling with relatively coarse spatial discretisation, keeping n_x small. Second, the iterative step count N_{it} typically remains $O(1)$. However, this efficiency comes with severe limitations: the step-size restriction prevents resolution of rapidly varying base flows or disturbance fields, excluding important physical phenomena from analysis.

OWNS-R exhibits substantially higher computational cost than PSE while remaining more efficient than full LHNS simulations. The increased expense arises from two factors. Without a modal ansatz, OWNS-R requires fine spatial resolution to capture disturbance structure: literature reports n_x values 10 to 60 times larger than PSE requirements [14]. Additionally, the recursion parameter count N_β typically exceeds N_{it} by an order of magnitude. Consequently, OWNS-R computations can be 100–600 times more intensive than equivalent PSE calculations.

Whilst M-OWNS might initially appear more demanding than OWNS-R for equivalent parameters (n_x , N_β , and $N_{\text{it}} > 1$), the modal ansatz and adaptive iteration enable dramatic reductions in required spatial resolution. Every case presented in this work achieves accurate results with n_x values only 2–3 times the PSE limit, representing a reduction of several orders of magnitude compared to OWNS-R requirements.

These results suggest that adaptive mesh refinement strategies could further enhance M-OWNS efficiency. By dynamically adjusting spatial resolution based on local disturbance characteristics, fine meshes near non-modal regions, coarser meshes elsewhere, computational resources could be optimally allocated. Such M-OWNS implementations represent a promising

avenue for future development, potentially enabling efficient stability analysis of even more complex three-dimensional flows.

5 Conclusions

We have introduced M-OWNS, a novel approach that overcomes the computational and convergence challenges inherent in traditional OWNS-R and PSE methods. Overall, the modal form of OWNS represents a significant advance in boundary layer stability analysis. Unlike PSE, M-OWNS has no minimum step-size restriction and models the full disturbance field without neglecting the streamwise pressure derivative, yielding more physically accurate solutions. The M-OWNS technique thus overcomes the historical minimum step-size limitation of PSE, combining the computational efficiency of modal methods with the physical completeness of non-modal approaches. In contrast to traditional OWNS, which requires extremely fine discretisations to resolve disturbances, M-OWNS leverages an adaptive iteration procedure together with the modal ansatz, substantially relaxing resolution requirements. This not only simplifies recursion parameter selection but also produces significant computational advantages, with costs scaling approximately as N_β and n_x step discretisations.

By permitting larger step-sizes without sacrificing accuracy, M-OWNS effectively captures both modal and non-modal disturbances across a wide range of flow configurations; from subsonic to supersonic boundary layers. M-OWNS also implicitly includes the ability to capture multimodal interactions. Our validations demonstrate that M-OWNS achieves accuracy comparable to full OWNS calculations whilst requiring 10–50 times fewer streamwise grid points, substantially reducing computational costs and mitigating numerical instabilities that plague OWNS-R at intermediate resolutions. Furthermore, its robust performance in resolving complex disturbance interactions, including transient growth, modal synchronisation, and acoustic radiation, makes it particularly suited for addressing receptivity problems in fluid flows. We believe that many forced problems of the type investigated by Ma and Zhong [41, 42, 44] using DNS can be modelled much more efficiently using the modal-OWNS approach presented here. More exhaustive investigations of forced problems are reported by Badcock [45].

Whilst the computational cost of OWNS-R scales with both the number of recursion parameters and discretisation points, M-OWNS offers significant efficiency gains. M-OWNS is typically 5 to 30 times faster than traditional OWNS-R, while maintaining the necessary resolution for both modal disturbances and complex non-modal transient growth phenomena. Our findings reveal that PSE’s difficulties in modelling non-modal disturbances stem primarily from its step-size limitation rather than from the modal ansatz itself. The weighted-average wavenumber formulation provides sufficient flexibility for the shape function to represent superpositions of multiple modes, challenging conventional understanding about modal method limitations. All M-OWNS computations reported in this paper were performed on standard desktop hardware, underscoring the practical accessibility of this approach.

Acknowledgements. We thank Dr J. Coppin of the United Kingdom’s Defence Science and Technology Laboratory (DSTL) for interest in this research and arranging funding support.

Declarations

- Competing interests: This work was supported by the United Kingdom Defence Science and Technology Laboratory (DSTL), under contract DSTLX1000152974
- Author contribution: Both authors contributed to the study conception and design. Material preparation, data collection and analysis were performed by E. Badcock. The first draft of the manuscript was written by E. Badcock and both authors commented on previous versions of the manuscript. Both authors have read and approved the final manuscript.

Appendix A Body-fitted compressible Navier-Stokes equations

The analysis begins with a surface in the Cartesian plane (x_1, x_2, x_3) , characterised by the function $x = x(x_1, x_2)$. We define a body-fitted orthogonal coordinate system such that x represents the streamwise direction aligned normal to a wing's leading edge, with increasing x corresponding to increasing of x_1 . The y axis is oriented orthogonally to the surface at each point in the (x_1, x_2) plane, while the z axis is positioned orthogonally to the surface relative to both x and y directions. t represents time. The general metric quantity of the coordinate system, denoted by $\chi(x, y)$, is formulated as

$$\chi(x, y) = \frac{1}{1 - y\kappa(x)}, \quad (\text{A1})$$

wherein $\kappa = \theta_x$ is the streamwise curvature, with θ representing the angle between the x_1 and x directions.

This research focuses on boundary layer flows of an ideal gas, delineated by specific freestream parameters: velocity U_∞^* , temperature T_∞^* , density ρ_∞^* , and dynamic viscosity μ_∞^* over a surface. The spatial dimensions are normalised with respect to the boundary layer thickness at the initial streamwise location on the surface. The non-dimensional body-fitted Navier-Stokes equations are then:

$$\bar{\rho}_t + \chi \bar{u} \bar{\rho}_x + \bar{v} \bar{\rho}_y + \bar{w} \bar{\rho}_z + \bar{\rho} (\chi \bar{u}_x + \bar{v}_y + \bar{w}_z - \kappa \chi \bar{v}) = 0, \quad (\text{A2})$$

$$\begin{aligned} \bar{\rho} (\bar{u}_t + \chi \bar{u} \bar{u}_x + \bar{v} \bar{u}_y + \bar{w} \bar{u}_z - \kappa \chi \bar{u} \bar{v}) &= -\chi \bar{p}_x \\ &+ \frac{1}{R} \left[\bar{\mu}_x \left[(m+2) \chi^2 (\bar{u}_x - \kappa \bar{v}) + m \chi (\bar{v}_y + \bar{w}_z) \right] + \bar{\mu}_y [\bar{u}_y + \chi (\bar{v}_x + \kappa \bar{u})] + \bar{\mu}_z (\bar{u}_z + \chi \bar{w}_x) \right. \\ &\left. + \bar{\mu} \left[(m+2) \chi^2 (\bar{u}_{xx} - \kappa \bar{v}_x) + (\bar{u}_y - \kappa \chi \bar{u}_y) + \bar{u}_{zz} + (m+1) \chi (\bar{v}_{xy} + \bar{w}_{xz}) - \kappa \chi^2 (\bar{v}_x + \kappa \bar{u}) \right] \right], \end{aligned} \quad (\text{A3})$$

$$\begin{aligned}
& \bar{\rho} (\bar{v}_t + \chi \bar{u} \bar{v}_x + \bar{v} \bar{v}_y + \bar{w} \bar{v}_z + \kappa \chi \bar{u}^2) = -\bar{p}_y \\
& + \frac{1}{R} \left[\bar{\mu}_x [\chi \bar{u}_y + \chi^2 (\bar{v}_x + \kappa \bar{u})] + \bar{\mu}_y [(m+2) \bar{v}_y + m \chi (\bar{u}_x - \kappa \bar{v}) + m \bar{w}_z] + \bar{\mu}_z [\bar{w}_y + \bar{v}_z] \right. \\
& \left. + \bar{\mu} [\chi^2 \bar{v}_{xx} + (m+2) (\bar{v}_{yy} - \kappa \chi \bar{v}_y) + \bar{v}_{zz} + (m+2) \kappa \chi^2 (\bar{u}_x - \kappa \bar{v}) + \kappa \chi^2 \bar{u}_x \right. \\
& \left. + (m+1) (\chi \bar{u}_{xy} + \bar{w}_{yz})] \right], \tag{A4}
\end{aligned}$$

$$\begin{aligned}
& \bar{\rho} (\bar{w}_t + \chi \bar{u} \bar{w}_x + \bar{v} \bar{w}_y + \bar{w} \bar{w}_z) = -\bar{p}_z \\
& + \frac{1}{R} \left[\bar{\mu}_x [\bar{u}_z + \chi \bar{w}_x] + \bar{\mu}_y [\bar{v}_z + \bar{w}_y] + \bar{\mu}_z [(m+2) \bar{w}_z + m \bar{v}_y + m \chi (\bar{u}_x - \kappa \bar{v})] \right. \\
& \left. + \bar{\mu} [\chi^2 \bar{w}_{xx} + \bar{w}_y + (m+2) \bar{w}_{zz} - \kappa \chi \bar{w}_y + (m+1) \bar{v}_{yz} + (m+1) \chi (\bar{u}_{xz} - \kappa \bar{v}_z)] \right], \tag{A5}
\end{aligned}$$

$$\begin{aligned}
& \bar{\rho} (\bar{T}_t + \chi \bar{u} \bar{T}_x + \bar{v} \bar{T}_y + \bar{w} \bar{T}_z) = (\gamma - 1) M^2 (\bar{p}_t + \chi \bar{u} \bar{p}_x + \bar{v} \bar{p}_y + \bar{w} \bar{p}_z) + \frac{(\gamma - 1) M^2}{R} \bar{\mu} \mathcal{D} \\
& + \frac{1}{\sigma R} (\chi^2 \bar{\mu}_x \bar{T}_x + \bar{\mu}_y \bar{T}_y + \bar{\mu}_z \bar{T}_z + \bar{\mu} (\chi^2 \bar{T}_{xx} + \bar{T}_y + \bar{T}_{zz} - \kappa \chi \bar{T}_y)), \tag{A6}
\end{aligned}$$

where

$$\begin{aligned}
\mathcal{D} = & (m+2) \left(\bar{w}_z^2 + [\bar{v}_y + \chi (\bar{u}_x - \kappa \bar{v})]^2 \right) + 2m (\bar{v}_y \bar{w}_z + \chi (\bar{u}_x \bar{w}_z - \kappa \bar{v} \bar{w}_z)) \\
& + 2 (\chi \bar{u}_z \bar{w}_x + \chi \bar{u}_y \bar{v}_x + \bar{v}_z \bar{w}_y) + \chi^2 (\bar{v}_x^2 + \bar{w}_x^2) + 4\chi (\kappa \bar{v} \bar{v}_y - \bar{u}_x \bar{v}_y) \\
& + 2\kappa (\bar{u} \bar{u}_y + \bar{u} \bar{v}_x) + \bar{u}_y^2 + \bar{w}_y^2 + \bar{u}_z^2 + \bar{v}_z^2 + \kappa^2 \chi^2 \bar{u}^2. \tag{A7}
\end{aligned}$$

\bar{u} , \bar{v} , and \bar{w} represent the streamwise, wall-normal, and spanwise velocities, respectively. \bar{T} represents temperature, $\bar{\rho}$ the density, \bar{p} the pressure, and $\bar{\mu}$ the viscosity. The system is characterised by several dimensionless parameters: γ denotes the ratio of specific heats, m represents the ratio of first and second viscosities, σ is the Prandtl number, R is the Reynolds number based on the boundary layer thickness at the initial streamwise location, and M represents the freestream Mach number. \mathcal{D} signifies the viscous dissipation. The system is closed using the ideal gas law,

$$\bar{p} = \frac{\bar{T} \bar{\rho}}{\gamma M^2}, \tag{A8}$$

and by expressing the viscosity as a function of temperature via Sutherland's law $\bar{\mu} = \bar{\mu}(\bar{T})$.

References

- [1] Theofilis, V.: Global linear instability. *Annual Review of Fluid Mechanics* **43**(Volume 43, 2011), 319–352 (2011) <https://doi.org/10.1146/annurev-fluid-122109-160705>
- [2] Appel, T.: Boundary layer instabilities due to surface irregularities: A harmonic navier-stokes approach. PhD thesis, Imperial College London (2021). <https://doi.org/10.25560/88722>
- [3] Herbert, T.: Boundary-layer transition-analysis and prediction revisited. In: 29th Aerospace Sciences Meeting, Reno, NV, USA (1991). <https://doi.org/10.2514/6.1991-737> . AIAA Paper 1991-737
- [4] Li, F., Malik, M.R.: On the nature of pse approximation. *Theor. Comput. Fluid Dyn.* **8**, 253–273 (1996) <https://doi.org/10.1007/BF00639695>
- [5] Li, F., Malik, M.R.: Spectral analysis of parabolized stability equations. *Computers and Fluids* **26**(3), 279–297 (1997) [https://doi.org/10.1016/S0045-7930\(96\)00044-8](https://doi.org/10.1016/S0045-7930(96)00044-8)
- [6] Andersson, P., Henningson, D., Hanifi, A.: On a stabilization procedure for the parabolic stability equations. *Journal of Engineering Mathematics* **33**, 311–332 (1998) <https://doi.org/10.1023/A:1004367704897>
- [7] Herbert, T., Bertolotti, F.P.: Stability analysis of nonparallel boundary layers. *Am. Phys. Soc.* **32**, 2079 (1987)
- [8] Towne, A., Rigas, G., Colonius, T.: A critical assessment of the parabolized stability equations. *Theor. Comput. Fluid Dyn.* **33**, 359–382 (2019) <https://doi.org/10.1007/s00162-019-00498-8>
- [9] Turner, M.R., Hammerton, P.W.: Asymptotic receptivity analysis and the parabolized stability equation: A combined approach to boundary layer transition. *Journal of Fluid Mechanics* **562**, 355–381 (2006) <https://doi.org/10.1017/S0022112006001108>
- [10] Towne, A., Colonius, T.: Improved parabolization of the euler equations. In: 19th AIAA/CEAS Aeroacoustics Conference, Berlin, Germany (2013). <https://doi.org/10.2514/6.2013-2171> . AIAA Paper 2013-2171
- [11] Towne, A., Colonius, T.: Continued development of the one-way euler equations: Application to jets. In: 20th AIAA/CEAS Aeroacoustics Conference, Atlanta, GA, USA (2014). <https://doi.org/10.2514/6.2014-2903> . AIAA Paper 2014-2903
- [12] Towne, A., Colonius, T.: One-way spatial integration of hyperbolic equations. *Journal of Computational Physics* **300**, 844–861 (2015) <https://doi.org/10.1016/j.jcp.2015.08.015>
- [13] Rigas, G., Schmidt, O.T., Colonius, T., Brés, G.A.: One-way navier–stokes and resolvent analysis for modeling coherent structures in a supersonic turbulent jet. In: 23rd AIAA/CEAS Aeroacoustics Conference, Denver, CO, USA (2017). <https://doi.org/10.2514/6.2017-2023>

- [14] Zhu, M., Towne, A.: Recursive one-way Navier-Stokes equations with PSE-like cost. *Journal of Computational Physics* **473**, 111744 (2023) <https://doi.org/10.1016/j.jcp.2022.111744>
- [15] Sleeman, M.K., Colonius, T.: Greedy recursion parameter selection for the One-Way Navier-Stokes (OWNS) equations (2025). <https://arxiv.org/abs/2506.02320>
- [16] Gao, B., Park, D.H., Park, S.O.: Stability analysis of a boundary layer over a hump using parabolized stability equations. *Fluid Dynamics Research* **43**(5), 055503 (2011) <https://doi.org/10.1088/0169-5983/43/5/055503>
- [17] Mughal, M.S., Ashworth, R.A.: Uncertainty quantification based receptivity modelling of crossflow instabilities induced by distributed surface roughness in swept wing boundary layers. In: 43rd AIAA Fluid Dynamics Conference, San Diego, CA, USA (2013). <https://doi.org/10.2514/6.2013-3106> . AIAA Paper 2013-3106
- [18] Badcock, E.J., Mughal, S.: Application of the One-Way Navier-Stokes Equations to Model Disturbance Evolution in Laminar Separation Bubbles. In: Kato, K., Inasawa, A., Matsubara, M. (eds.) *Proceedings of the 10th IUTAM Symposium on Laminar-Turbulent Transition*, vol. 44, p. 284. Springer, Nagano, Japan (2025). In press
- [19] Mughal, M.S.: Active control of wave instabilities in three-dimensional compressible flows. *Theor. Comput. Fluid Dyn.* **12**, 195–217 (1998) <https://doi.org/10.1007/s001620050106>
- [20] Haj-Hariri, H.: Characteristics analysis of the parabolized stability equations. *Studies in Applied Mathematics* **92**(1), 41–53 (1994) <https://doi.org/10.1002/sapm199492141>
- [21] Schmid, P.J.: Nonmodal Stability Theory. *Annual Review of Fluid Mechanics* **39** (Volume 39, 2007), 129–162 (2007) <https://doi.org/10.1146/annurev.fluid.38.050304.092139>
- [22] Hanifi, A., Schmid, P.J., Henningson, D.S.: Transient growth in compressible boundary layer flow. *Physics of Fluids* **8**(3), 826–837 (1996) <https://doi.org/10.1063/1.868864>
- [23] Schmid, P.J., Henningson, D.S.: Stability and Transition in Shear Flows. *Applied Mathematical Sciences*, vol. 142. Springer, New York, NY (2001). <https://doi.org/10.1007/978-1-4613-0185-1>
- [24] Mack, L.M.: Boundary-layer linear stability theory. In: AGARD Special Course on Stability and Transition of Laminar Flow, pp. 3–181. AGARD Report R-709, Neuilly-sur-Seine, France (1984)
- [25] Malik, M.R.: Numerical methods for hypersonic boundary layer stability. *Journal of Computational Physics* **86**(2), 376–413 (1990) [https://doi.org/10.1016/0021-9991\(90\)90106-B](https://doi.org/10.1016/0021-9991(90)90106-B)

- [26] Guo, Y., Malik, M., Chang, C.-L.: A solution adaptive approach for computation of linear waves. In: 13th AIAA Computational Fluid Dynamics Conference, Snowmass Village, CO, USA (1997). <https://doi.org/10.2514/6.1997-2072> . AIAA Paper 1997-2072
- [27] Franco Sumariva, J.A., Hein, S.J.: Adaptive harmonic linearized navier–stokes equations used for boundary layer instability analysis in the presence of large streamwise gradients. In: AIAA Aerospace Sciences Meeting, Kissimmee, FL, USA (2018). <https://doi.org/10.2514/6.2018-1548> . AIAA Paper 2018-1548
- [28] Chuvakhov, P.V., Fedorov, A.V.: Spontaneous radiation of sound by instability of a highly cooled hypersonic boundary layer. *Journal of Fluid Mechanics* **805**, 188–206 (2016) <https://doi.org/10.1017/jfm.2016.560>
- [29] Kamal, O., Rigas, G., Lakebrink, M.T., Colonius, T.: Input/output analysis of a mach-6 cooled-wall hypersonic boundary layer using the one-way navier-stokes ownsequations. In: AIAA AVIATION 2022 Forum. AIAA Paper 2022-3556, ??? (2022). <https://doi.org/10.2514/6.2022-3556>
- [30] Briggs, R.J.: Electron-Stream Interaction with Plasmas. The MIT Press, ??? (1964). <https://doi.org/10.7551/mitpress/2675.001.0001>
- [31] Towne, A.S.: Advancements in jet turbulence and noise modeling: Accurate one-way solutions and empirical evaluation of the nonlinear forcing of wavepackets. PhD thesis, California Institute of Technology (2016). <https://doi.org/10.7907/Z99884XJ>
- [32] Towne, A., Rigas, G., Kamal, O., Pickering, E., Colonius, T.: Efficient global resolvent analysis via the one-way navier-stokes equations. *Journal of Fluid Mechanics* **948** (2022) <https://doi.org/10.1017/jfm.2022.647>
- [33] Rudel, C., Pernet, S., Brazier, J.-P.: Numerical Factorization of Propagation Operator for Hyperbolic Equations and Application to One-way, True Amplitude One-way Equations and Bremmer Series. *Journal of Scientific Computing* **93**(1), 27 (2022) <https://doi.org/10.1007/s10915-022-01985-7>
- [34] Thompson, K.W.: Time dependent boundary conditions for hyperbolic systems. *Journal of Computational Physics* **68**(1), 1–24 (1987) [https://doi.org/10.1016/0021-9991\(87\)90041-6](https://doi.org/10.1016/0021-9991(87)90041-6)
- [35] Balakumar, P., Malik, M.R.: Discrete modes and continuous spectra in supersonic boundary layers. *Journal of Fluid Mechanics* **239**, 631–656 (1992) <https://doi.org/10.1017/S0022112092004555>
- [36] Fedorov, A.: Transition and Stability of High-Speed Boundary Layers. *Annual Review of Fluid Mechanics* **43**(1), 79–95 (2011) <https://doi.org/10.1146/annurev-fluid-122109-160750>
- [37] Malik, M.R., Li, F., Chang, C.-L.: Crossflow disturbances in three-dimensional boundary

layers: Nonlinear development, wave interaction and secondary instability. *Journal of Fluid Mechanics* **268**, 1–36 (1994) <https://doi.org/10.1017/S0022112094001242>

[38] Fedorov, A.V.: Receptivity of a high-speed boundary layer to acoustic disturbances. *Journal of Fluid Mechanics* **491**, 101–129 (2003) <https://doi.org/10.1017/S0022112003005263>

[39] Fedorov, A., Tumin, A.: Branching of discrete modes in high-speed boundary layers and terminology issues. In: 40th Fluid Dynamics Conference and Exhibit. AIAA Paper 2010-5003, Chicago, Illinois (2010). <https://doi.org/10.2514/6.2010-5003>

[40] Fedorov, A., Tumin, A.: High-speed boundary-layer instability: Old terminology and a new framework. *AIAA Journal* **49**(8), 1647–1657 (2011) <https://doi.org/10.2514/1.J050835>

[41] Ma, Y., Zhong, X.: Numerical simulation of receptivity and stability of nonequilibrium reacting hypersonic boundary layers. In: 39th Aerospace Sciences Meeting and Exhibit. AIAA Paper 2001-892, Reno, NV, U.S.A. (2001). <https://doi.org/10.2514/6.2001-892>

[42] Ma, Y., Zhong, X.: Receptivity of a supersonic boundary layer over a flat plate. Part 1. Wave structures and interactions. *Journal of Fluid Mechanics* **488**, 31–78 (2003) <https://doi.org/10.1017/S0022112003004786>

[43] Ma, Y., Zhong, X.: Receptivity of a supersonic boundary layer over a flat plate. Part 2. Receptivity to free-stream sound. *Journal of Fluid Mechanics* **488**, 79–121 (2003) <https://doi.org/10.1017/S0022112003004798>

[44] Ma, Y., Zhong, X.: Receptivity of a supersonic boundary layer over a flat plate. Part 3. Effects of different types of free-stream disturbances. *Journal of Fluid Mechanics* **532**, 63–109 (2005) <https://doi.org/10.1017/S0022112005003836>

[45] Badcock, E.J.: Modal one-way navier-stokes: Efficient spatial marching for modal and non-modal boundary layer disturbances. PhD thesis, Imperial College London (2025). PhD thesis, in preparation